*energies*

MDPI

*Article*

# A Parametric Study of a Fully Passive Oscillating Foil Turbine on a Swinging Arm in a Tandem Configuration

**Dominic Cloutier, Mathieu Olivier and Guy Dumas ***

CFD Laboratory LMFN, Département de Génie Mécanique, Université Laval, Québec, QC G1V 0A6, Canada; dominic.cloutier.3@ulaval.ca (D.C.); mathieu.olivier@gmc.ulaval.ca (M.O.)
* Correspondence: gdumas@gmc.ulaval.ca

**Abstract**

A fully passive oscillating foil turbine on a swinging arm in a tandem configuration consisting of two NACA 0015 foils at both ends of its arm and operating in an incompressible flow at a Reynolds number of $3.9 \times 10^6$ is investigated with numerical simulations. The turbine is free to oscillate passively in response to hydrodynamic forces and structural reactions from springs and dampers. The passive motion of the tandem turbine arises from a transfer of energy from the flow, and this motion is solved using a fluid-structure algorithm coupling the Newtonian dynamics of the system with two-dimensional, unsteady, and Reynolds-averaged Navier–Stokes equations. The performance metrics, i.e., the efficiency and power coefficient, of the proposed turbine concept are explored with a momentum gradient ascent algorithm, which uses the near-optimal configuration of an equivalent single-foil concept from a previous study as a starting point. These starting configurations consist of tandem foils operating either under coupled flutter or stall flutter instabilities. The use of gears to adjust the equilibrium position of the pitching motion is also considered, resulting in a total of four baseline configurations. The best configuration found with the gradient ascent algorithm presents an efficiency value near 75% and a power coefficient of 1.46, showing the great potential of fully passive oscillating foil turbines operating in a tandem configuration and providing valuable insight for further development of this technology through three-dimensional simulations and prototype testing.

**Keywords:** renewable energy; CFD; turbine; fully passive; oscillating foil; tandem; URANS

check for updates

Academic Editor: Davide Astolfi

Received: 29 March 2025
Revised: 24 May 2025
Accepted: 16 June 2025
Published: 21 June 2025

**Citation:** Cloutier, D.; Olivier, M.; Dumas, G. A Parametric Study of a Fully Passive Oscillating Foil Turbine on a Swinging Arm in a Tandem Configuration. *Energies* **2025**, *18*, 3253. https://doi.org/10.3390/en18133253

**Copyright:** © 2025 by the authors. Licensee MDPI, Basel, Switzerland. This article is an open access article distributed under the terms and conditions of the Creative Commons Attribution (CC BY) license (https://creativecommons.org/licenses/by/4.0/).

## 1. Introduction

Fully constrained oscillating foil turbines have been extensively studied in the last two decades [1–7] and, to a lesser extent, their fully passive counterparts, as reported in a recent survey by Liu et al. [1]. Though proven to be a very promising concept through numerical studies [8–10] and experimentations [2,3,11,12], the mechanical complexity of the constrained versions poses a considerable problem. To simplify the mechanical complexity and friction losses of such turbines, the idea of leveraging the passive motion of an elastically mounted foil has been investigated [13–18]. Through the judicious use of springs, dampers, and masses, the motion of the fully passive oscillating foil turbine (FP-OFT) is only determined by hydrodynamic forces acting on the foil and counteracted by said springs and dampers. Efficiency values of 51.0% and 33.6% have been reported by 2D URANS numerical simulations for the FP-OFT operating under coupled flutter [16] and stall flutter [13] instabilities, respectively. In these previous studies, the heaving motion was guided by straight rails and was thus linear in contrast to the heaving motion, resulting in

a pivoting arm. In this study, we use the term "linear heaving" to refer to the railed design. The potential of these fully passive foils was confirmed through experimental studies, though lower performances were obtained [14,15,18]. This is to be expected since the inherent physical complexity of the real 3D flows in confined channels is quite simplified in 2D URANS simulations.

Several studies have considered an oscillating foil turbine on a swinging arm, both numerically [19–21] and experimentally [22–24]. However, no studies have compared the scaling factor between the parameters of a fully passive oscillating foil turbine on a swinging arm (FP-OFT-SA) with varying arm lengths and those of an FP-OFT undergoing linear heaving. This was an important focus of our previous work [25], in which several configurations were analyzed, with the foil being either upstream or downstream of the arm and with or without the use of gears to assign a specific resting position to the pitch spring of the foil. That study revealed comparable key performance indicators to those of linearly heaving FP-OFTs that were even better in some cases. Indeed, the geared turbine operating under the coupled flutter instability achieved an efficiency near 55%. The reader is strongly encouraged to consult our recent prior work [25] on which the present paper is based.

With conclusive and encouraging results, the next step was to include two foils, one on each end of the arm, and to assess how both fully passive foils could interact in tandem to extract energy from the same extraction window. The presence of an upstream foil could create a complex wake, making it unclear whether a fully passive tandem configuration could operate with stability and efficiency. Indeed, this paper aims to demonstrate that such a scenario exists.

Literature concerning fully passive oscillating foil turbines on a swinging arm in a tandem configuration (FP-OFT-SAT) such as the one in this study is, to the best of the authors' knowledge, non-existent. Indeed, Kinsey and Dumas experimentally studied a 2 kW prototype of the tandem configuration of the constrained OFT [3], obtaining an efficiency value of 40%, in good agreement with their CFD study [9]. In more recent years, other studies, such as the experimental works by Zhao et al. [26] and Wang and Ng [27], used a fully passive configuration designed with heave and pitch limiters, rather than springs and dampers, to produce cyclical motions. These tandem configurations, reaching efficiency values of about 20% and 40%, respectively, were, again, not connected on a swinging arm but with two foils placed in series in an incoming flow. Zhao et al. [28] used a semi-passive approach prescribing the pitching motion of two foils placed in series in an incoming flow, reaching an efficiency value of 16%. Qu and Liu [29] also used a semi-passive concept prescribing the pitching motion of two foils again but on two distinct swinging arms connected at the same pivot point. Being able to control the global phase shift with the use of two separate arms, they obtained a maximum efficiency value of 69%.

A novel design of the vertical axis wind turbine (VAWT) was studied by Naccache and Paraschivoiu [30,31]. In their design of a dual vertical-axis wind turbine (D-VAWT), they proposed the use of two foils heaving in tandem by extending the maximum power region of a classical H-rotor Darrieus turbine to increase the overall efficiency. With this dual heaving motion, somewhat resembling that of this current study, they obtained a power coefficient of 0.604 using 2D CFD. Therefore, in the absence of numerical and experimental investigation on the FP-OFT-SAT using a single swinging arm and only springs and dampers to obtain fully passive motions, the present study aims to shed light on this novel turbine concept and to demonstrate that it can operate regularly and with some robustness while producing competitive efficiency. To evaluate the performance of this concept, 2D URANS CFD simulations are conducted to determine its efficiency and power coefficient. These simulations are performed in conditions where the turbine is

operating under either the coupled flutter or stall flutter instability, as well as with and without gear systems to control the rest position of the foils' pitch springs.

## 2. Methodology

### *2.1. Dynamics*

In order to compare the performances of the tandem configuration to those of the single foil one studied in [25], the same flow conditions were used, such as the chord-based Reynolds number:

$$\mathrm{Re}_c = \frac{U_\infty c}{\nu} = 3.9 \times 10^6. \tag{1}$$

A FP-OFT-SAT is comprised of two foils placed at the extremities of a single rigid arm. The two foils are free to rotate in pitch, and the arm is free to rotate about pivot axis $Q$, as is shown in Figure 1. Note that both pivot points $P_1$ and $P_2$ are at the same distance from their blade's leading edge, which can be either $c/3$ for the stall flutter cases or $c/4$ for the coupled flutter cases (see Table 1 further below).

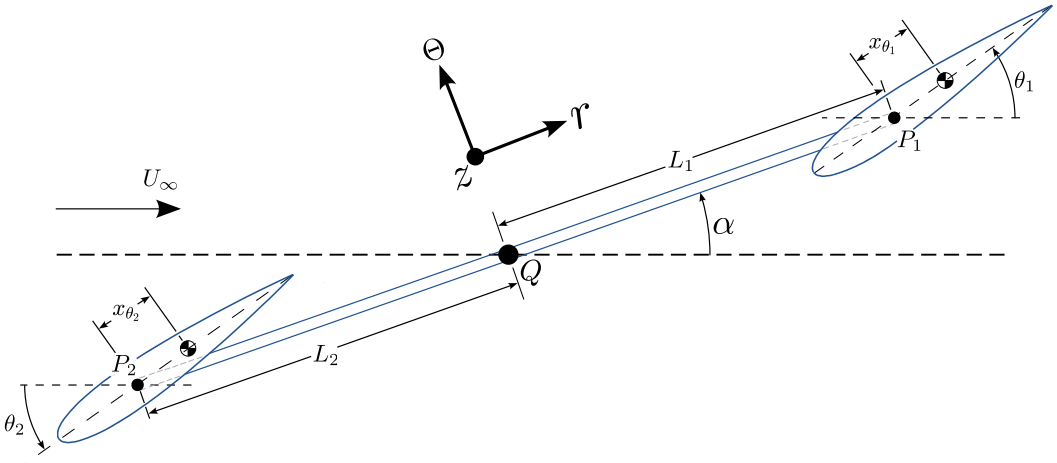



**Figure 1.** Schematic of the FP-OFT-SAT. For simplicity, springs and dampers at pivots $P_1$, $P_2$, and $Q$ are not shown (gravity acts in the $z$-direction).

All movements are only passively restricted by springs and dampers and are, therefore, not imposed by sine functions such as those governing the pitch and heave motions of the fully constrained oscillating foil turbine studied by Kinsey and Dumas [9]. As was the case for the FP-OFT-SA in our preliminary work [25], the turbine can either be geared or gearless in order to control or not control the resting position of the pitch springs of the foils and to decouple the pitch degrees of freedom from the dynamics of the arm (see Figure 2). The study on the FP-OFT-SA showed that the geared configuration is better suited for optimal performances but that the gearless configuration can be optimized in order to produce reasonably good performances when compared to its geared counterpart. Thus, in this paper, we analyze both the geared and gearless configurations for the FP-OFT-SAT. This gives rise to two sets of equations of motion for the turbine, which use the following dimensionless parameters for independent variables:

$$L_i^* = \frac{L_i}{c}, \tag{2a}$$

$$k_{\theta_i}^* = \frac{k_{\theta_i}}{\rho U_\infty^2 b c^2}, \quad k_\alpha^* = \frac{k_\alpha}{\rho U_\infty^2 b c^2}, \tag{2b}$$

$$D_{\theta_i}^* = \frac{D_{\theta_i}}{\rho U_\infty b c^3}, \quad D_\alpha^* = \frac{D_\alpha}{\rho U_\infty b c^3}, \tag{2c}$$

$$I^*_{\theta_i} = \frac{I_{\theta_i}}{\rho b c^4}, \quad I^*_B = \frac{I_B}{\rho b c^4}, \tag{2d}$$

$$S^*_i = \frac{S_i}{\rho b c^3}, \tag{2e}$$

For dependent variables, the following are used:

$$\dot{\theta}^*_i = \frac{\dot{\theta}_i c}{U_\infty}, \quad \dot{\alpha}^* = \frac{\dot{\alpha} c}{U_\infty}, \tag{3a}$$

$$\ddot{\theta}^*_i = \frac{\ddot{\theta}_i c^2}{U^2_\infty}, \quad \ddot{\alpha}^* = \frac{\ddot{\alpha} c^2}{U^2_\infty}, \tag{3b}$$

$$C_{M_i} = \frac{M_i}{0.5 \rho U^2_\infty b c^2}, \tag{3c}$$

$$C_{F_{y_i}} = \frac{F_{y_i}}{0.5 \rho U^2_\infty b c}, \quad C_{F_{x_i}} = \frac{F_{x_i}}{0.5 \rho U^2_\infty b c}, \tag{3d}$$

where the index $i$ designates the downstream foil ($i = 1$) or the upstream foil ($i = 2$), $L_i$ is the length of the swinging arm in the upstream or downstream direction, $\theta_i$ is the pitch angle of one of the foils, $\alpha$ is the angular position of the arm, $k_{\theta_i}$ is the stiffness of one of the foils' spring at point $P_i$, $k_\alpha$ is the stiffness of the arm's spring at point $Q$, $D_{\theta_i}$ is the coefficient of one of the foils' damper at point $P_i$, $D_\alpha$ is the coefficient of the arm's damper at point $Q$, $I_{\theta_i}$ is the moment of inertia of one of the foils measured at point $P_i$, $I_B$ is the combination of the moment of inertia of the arm measured at point $Q$ and the added masses $m_i$ of the foils at both ends of the arm, i.e., $I_B = I_Q + m_1 L^2_1 + m_2 L^2_2$, $S_i$ is the static imbalance taking into consideration the displacement of one of the foils' center of mass from point $P_i$, i.e., $S_i = m_i x_{\theta_i}$, $M_i$ is the hydrodynamic torque acting on one of the foils, $F_{y_i}$ and $F_{x_i}$ are the hydrodynamic forces acting on one of the foils, $\rho$ is the fluid density, $U_\infty$ is the freestream velocity, $c$ is the foils' chord length, and $b$ is the foils' span length. Both the span and chord lengths are identical for the two foils. Additionally, in this two-dimensional study, the foils' span length is assumed to be equal to unity for convenience ($b = 1$), and hydrodynamic forces on the arm are not considered.

Examining the FP-OFT-SAT by adding up the forces and moments on the two foils and the arm yields three equations that describe the dynamic behavior of the entire system. These equations connect the three degrees of freedom of the system: the two pitch angles of the foils, $\theta_1$ and $\theta_2$, and the swinging arm's angular position, $\alpha$. Again, from the possible geared or gearless configurations (see Figure 2), two sets of equations are obtained and hereby expressed with the dimensionless parameters previously presented.

**Geared:**

$$\begin{aligned} \frac{1}{2}\Big[L^*_1\Big[C_{F_{y_1}}\cos(\alpha) - C_{F_{x_1}}\sin(\alpha)\Big] - L^*_2\Big[C_{F_{y_2}}\cos(\alpha) - C_{F_{x_2}}\sin(\alpha)\Big]\Big] \\ = I^*_B\ddot{\alpha}^* + D^*_\alpha\dot{\alpha}^* + k^*_\alpha\alpha + S^*_1L^*_1\Big[\ddot{\theta}^*_1\cos(\theta_1 - \alpha) - \dot{\theta}^{*2}_1\sin(\theta_1 - \alpha)\Big] \\ - S^*_2L^*_2\Big[\ddot{\theta}^*_2\cos(\theta_2 - \alpha) - \dot{\theta}^{*2}_2\sin(\theta_2 - \alpha)\Big], \end{aligned} \tag{4a}$$

$$\frac{C_{M_1}}{2} = I^*_{\theta_1}\ddot{\theta}^*_1 + D^*_{\theta_1}\dot{\theta}^*_1 + k^*_{\theta_1}\theta_1 + S^*_1L^*_1\Big[\ddot{\alpha}^*\cos(\theta_1 - \alpha) + \dot{\alpha}^{*2}\sin(\theta_1 - \alpha)\Big], \tag{4b}$$

$$\frac{C_{M_2}}{2} = I^*_{\theta_2}\ddot{\theta}^*_2 + D^*_{\theta_2}\dot{\theta}^*_2 + k^*_{\theta_2}\theta_2 - S^*_2L^*_2\Big[\ddot{\alpha}^*\cos(\theta_2 - \alpha) + \dot{\alpha}^{*2}\sin(\theta_2 - \alpha)\Big]. \tag{4c}$$

**Gearless:**

$$\begin{aligned}&\frac{1}{2}\left[L_1^*\left[C_{F_{y_1}}\cos(\alpha)-C_{F_{x_1}}\sin(\alpha)\right]-L_2^*\left[C_{F_{y_2}}\cos(\alpha)-C_{F_{x_2}}\sin(\alpha)\right]\right]\\&=I_B^*\ddot{\alpha}^*+D_\alpha^*\dot{\alpha}^*+k_\alpha^*\alpha-D_{\theta_1}^*\left(\dot{\theta}_1^*-\dot{\alpha}^*\right)-k_{\theta_1}^*(\theta_1-\alpha)-D_{\theta_2}^*\left(\dot{\theta}_2^*-\dot{\alpha}\right)-k_{\theta_2}^*(\theta_2-\alpha)\\&+S_1^*L_1^*\left[\ddot{\theta}_1^*\cos(\theta_1-\alpha)-\dot{\theta}_1^{*2}\sin(\theta_1-\alpha)\right]-S_2^*L_2^*\left[\ddot{\theta}_2^*\cos(\theta_2-\alpha)-\dot{\theta}_2^{*2}\sin(\theta_2-\alpha)\right],\end{aligned}\tag{5a}$$

$$\begin{aligned}\frac{C_{M_1}}{2}&=I_{\theta_1}^*\ddot{\theta}_1^*+D_{\theta_1}^*\left(\dot{\theta}_1^*-\dot{\alpha}^*\right)+k_{\theta_1}^*(\theta_1-\alpha)\\&+S_1^*L_1^*\left[\ddot{\alpha}^*\cos(\theta_1-\alpha)+\dot{\alpha}^{*2}\sin(\theta_1-\alpha)\right],\end{aligned}\tag{5b}$$

$$\begin{aligned}\frac{C_{M_2}}{2}&=I_{\theta_2}^*\ddot{\theta}_2^*+D_{\theta_2}^*\left(\dot{\theta}_2^*-\dot{\alpha}^*\right)+k_{\theta_2}^*(\theta_2-\alpha)\\&-S_2^*L_2^*\left[\ddot{\alpha}^*\cos(\theta_2-\alpha)+\dot{\alpha}^{*2}\sin(\theta_2-\alpha)\right].\end{aligned}\tag{5c}$$

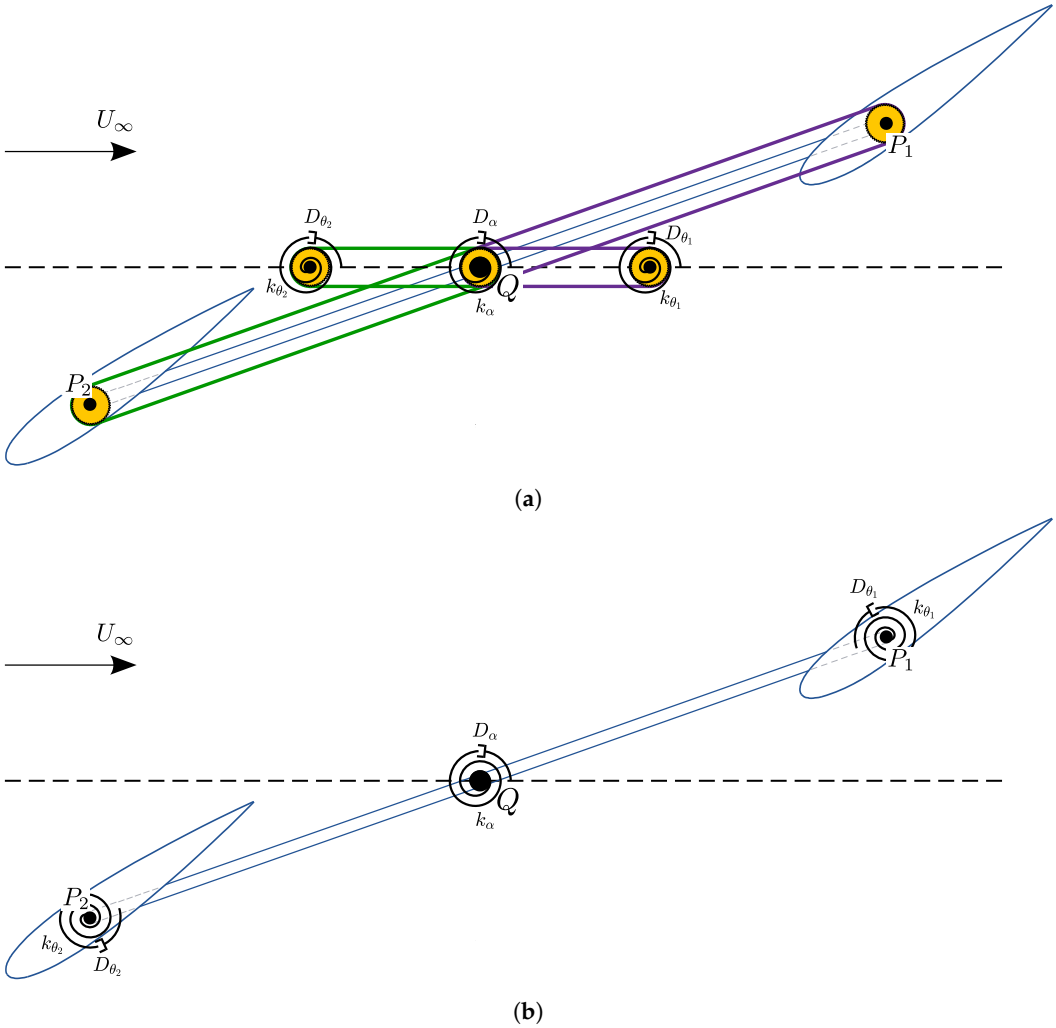



**Figure 2.** Schematic of the FP-OFT-SAT (**a**) with and (**b**) without gears.

### *2.2. Evaluating the Structural Parameters*

The structural parameters of the FP-OFT-SAT can be derived from an equivalent turbine undergoing linear heaving, as was carried out in [25]. This is accomplished by considering a small angular motion of the arm such that the heaving motion of the two foils is nearly linear. For instance, when looking at the torsional spring $k_\alpha$ at point $Q$, one can compare it to two linear springs $k_h$ placed at the extremities of the rigid arm.

With this idealization, illustrated in Figure 3, one can thus estimate that, for the same small angular position $\alpha$, the torque produced by spring $k_\alpha$ and the torques produced by the two springs $k_h$ are equal:

$$k_\alpha \alpha = k_h \left[ L_1^2 + L_2^2 \right] \alpha, \tag{6}$$

which gives

$$k_\alpha = k_h \left[ L_1^2 + L_2^2 \right]. \tag{7}$$

Similarly, the total inertia $I_B$ and the rotational damper $D_\alpha$ are related to the mass and damping of the equivalent linearly heaving configuration by the following:

$$I_B = m_h \left[ L_1^2 + L_2^2 \right], \tag{8}$$

$$D_\alpha = D_h \left[ L_1^2 + L_2^2 \right]. \tag{9}$$

A ratio $R$ is defined as the ratio of the downstream length $L_1$ to the total length $L_{tot} = L_1 + L_2$ of the arm. This choice of normalization is, of course, not unique and has been chosen to bound the value of $R$ between 0 and 1:

$$0 < R = \frac{L_1}{L_{tot}} < 1. \tag{10}$$

As is shown in Figure 4, when the pivot point $Q$ is placed in the middle of the arm, i.e., when $L_1 = L_2$, the ratio becomes $R = 0.5$. When $R = 0$ and $R = 1$, the turbine's configuration becomes that of an FP-OFT-SA using only a single foil, either upstream or downstream, respectively.

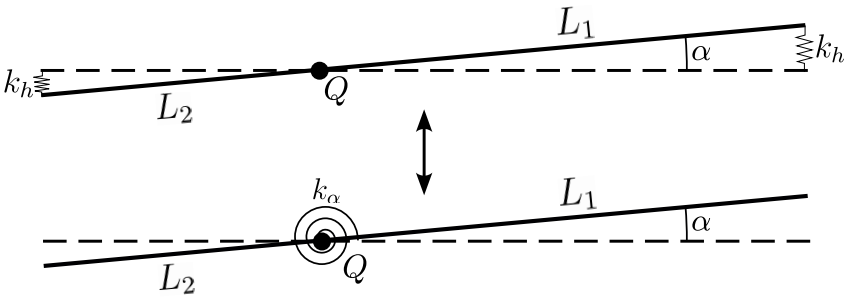



**Figure 3.** Schematic showing equivalent spring configurations between two linear springs and a single torsional spring at point $Q$.

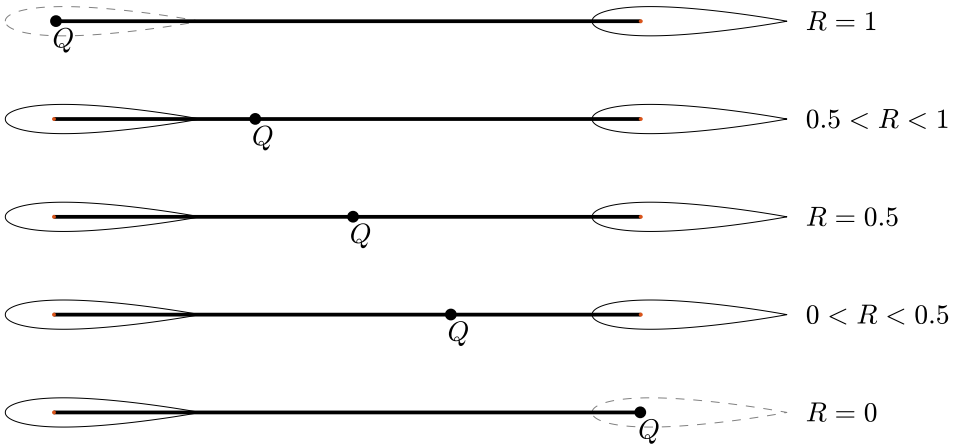



**Figure 4.** Ratio $R = \frac{L_1}{L_{tot}}$ defining the position of the pivot point $Q$ of the arm.

Using this parameter $R$, the scaling factor found in Equations (7)–(9) can now be expressed in terms of the total length $L_{tot}$ of the arm and the ratio $R$:

$$I_B = m_h L_{tot}^2 \left[R^2 + (1-R)^2\right], \tag{11}$$

$$D_\alpha = D_h L_{tot}^2 \left[R^2 + (1-R)^2\right], \tag{12}$$

$$k_\alpha = k_h L_{tot}^2 \left[R^2 + (1-R)^2\right]. \tag{13}$$

Consequently, considering the entire arm length and location of the hinge relative to the downstream end of the arm, Equations (11)–(13) can be used to determine equivalent values of the arm's structural parameters based on values readily accessible through previous studies on the FP-OFT [13,16] and on the FP-OFT-SA in [25]. These established values are presented in Table 1 and are used in this study to produce the initial configurations of the optimization procedure of the FP-OFT-SAT.

**Table 1.** Structural parameters of the best-reported FP-OFT configurations operating under coupled flutter and stall flutter instabilities from the literature and used here as the initial configurations.

| Parameter | Coupled Flutter (Boudreau et al. [16]) | Coupled Flutter (Cloutier et al. [25]) | Stall Flutter (Veilleux et al. [13]) |
|---|---|---|---|
| $x_p/c$ | 1/4 | 1/4 | 1/3 |
| $m_h^*$ | 2 | 9.981 | 3.036 |
| $D_h^*$ | 0.7 | 0.687 | 1.501 |
| $k_h^*$ | 1.55 | 14.048 | 1.206 |
| $I_\theta^*$ | 2 | 2 | 0.095 |
| $D_\theta^*$ | 0 | 0 | 0.119 |
| $k_\theta^*$ | 3.16 | 3.16 | 0.031 |
| $S^*$ | 0.65 | 0.65 | −0.029 |

### 2.3. Performance Metrics

The FP-OFT-SAT derives its power from three distinct sources: the two forces, $F_x$ and $F_y$, and the pitch torque, $M$. Naturally, each of these three sources is generated by two foils. By employing the dimensionless parameters discussed in Section 2.1, we can define the following power coefficients:

$$\langle C_{P_y} \rangle = \frac{1}{T^*} \int_{t_i^*}^{t_i^*+T^*} \left[C_{F_{y_1}} L_1^* - C_{F_{y_2}} L_2^*\right] \cos(\alpha) \dot{\alpha}^* \, dt^*, \tag{14}$$

$$\langle C_{P_x} \rangle = \frac{-1}{T^*} \int_{t_i^*}^{t_i^*+T^*} \left[C_{F_{x1}} L_1^* - C_{F_{x2}} L_2^*\right] \sin(\alpha) \dot{\alpha}^* \, dt^*, \tag{15}$$

$$\langle C_{P_\theta} \rangle = \frac{1}{T^*} \int_{t_i^*}^{t_i^*+T^*} \left[C_{M_1} \dot{\theta}_1^* + C_{M_2} \dot{\theta}_2^*\right] dt^*, \tag{16}$$

and the power coefficient of the entire turbine is determined as follows:

$$\langle C_P \rangle = \langle C_{P_y} \rangle + \langle C_{P_x} \rangle + \langle C_{P_\theta} \rangle, \tag{17}$$

where the angle brackets indicate cycle-averaged values, $t_i^*$ and $T^*$ are the initial dimensionless time ($t^* = tU_\infty/c$) and the dimensionless period of a given cycle once regular periodic cycles are reached, typically after 10 cycles from the start. For the remainder of the study, the term "power coefficient" refers to the cycle-averaged value unless otherwise specified.

The term "energy extraction efficiency" ($\eta$), often used in discussions on renewable energy, can be expressed as a fraction. It represents the relationship between two quantities: the average power generated by the turbine $\langle P \rangle$ and the kinetic energy flux contained in the moving fluid that interacts with the turbine's swept area:

$$\eta = \frac{\langle P \rangle}{1/2\,\rho U_\infty^3 bd}, \tag{18}$$

where $d$ represents the maximum total height of the power extraction window. This value corresponds to the highest and lowest points that one of the two foils reaches during a cycle as a result of the combined effects of both the heave and pitch amplitudes. This is shown in Figure 5.

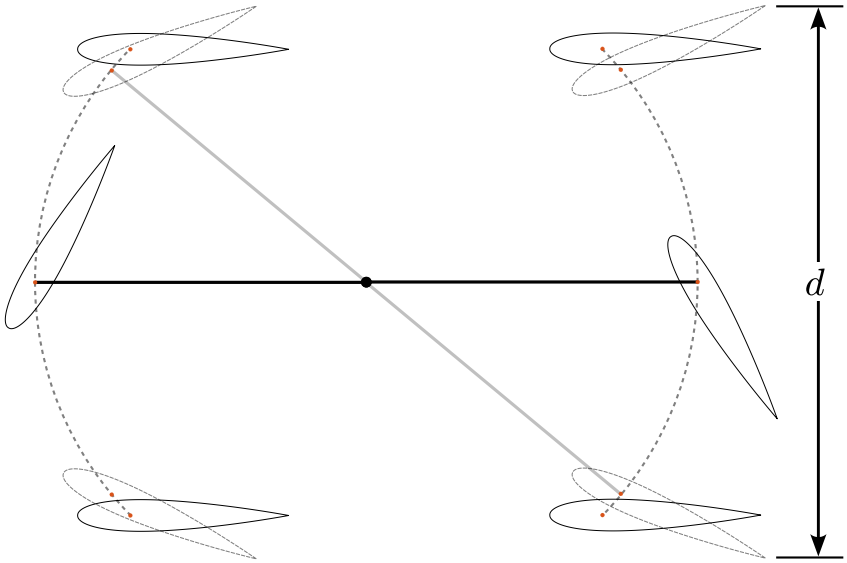



**Figure 5.** Height $d$ of the energy extraction window of an FP-OFT-SAT.

Indeed, even if the pivot point $Q$ is at the middle point of the arm, the downstream and upstream swept heights may vary slightly from one another because of the different pitch amplitudes of the two foils. However, the turbine is considered as a single unit, and only the overall maximum height is taken into account. Therefore, in this study, the value of $d$ in Equation (18) is taken as the maximum value between the two swept heights for a given cycle:

$$d = \max\{d_1; d_2\}. \tag{19}$$

### *2.4. Numerics*

#### 2.4.1. Fluid–Structure Interaction Algorithm

As was the case in our previous study of the FP-OFT-SA in [25], the fluid–structure interaction (FSI) simulations in this research were performed with an internally developed algorithm embedded in Siemens STAR-CCM+® software, version 2021.2, build 16.04.007-R8 [32]. The FSI algorithm is the same as the one used for the FP-OFT-SA in [25], where only the discretized equations of motions have been modified to correspond to those of the FP-OFT-SAT (Equations (4a)–(5c)), providing a system of three degrees of freedom. The fluid solver is also exactly identical to the one used for the study of the FP-OFT-SA [25]. Therefore, the convergence criteria, the boundary conditions and the inlet turbulent conditions are unchanged. Of course, all criteria pertaining to the single foil of the FP-OFT-SA [25] have been duplicated in order to apply the same criteria to the two foils of the FP-OFT-SAT independently.

2.4.2. Cfd Domain and Mesh

The CFD domain used in this study is presented in Figure 6. This domain has a fixed height of $100c$, and its width varies with respect to the total length of the arm. The total number of cells can, therefore, vary depending on the length of the arm. For instance, most of the simulations presented in this research were conducted using $L^*_{tot} = 5$, which corresponds to a total number of cells of 161,866. In all cases, a uniform velocity profile and a constant turbulent viscosity ratio of $\tilde{\nu}/\nu = 3$ are applied at the entrance (left edge). According to the suggestion of [33], this viscosity ratio guarantees that the Sparlart–Allmaras turbulence model operates in its fully turbulent regime. Furthermore, zero-gauge pressure is imposed on the outlet (right border), while symmetry conditions are applied to the top and bottom boundaries of the domain. Both the right and left borders are located at fixed distances of $50c$ of the refined zone in the middle of the domain. In the refined zone, two overset meshes are placed at their respective distances $(L^*_1, L^*_2)$ from the origin (arm's pivot point $Q$). These overset meshes are the same as those the authors used for the FP-OFT-SA in [25] and consist of 29,323 cells, and each foil has 500 nodes placed on its contour. All simulations used a time step such that $U_\infty \Delta t/c = 0.005$, yielding typically over 1000 time steps per cycle, which was verified to produce time-step-independent solutions.

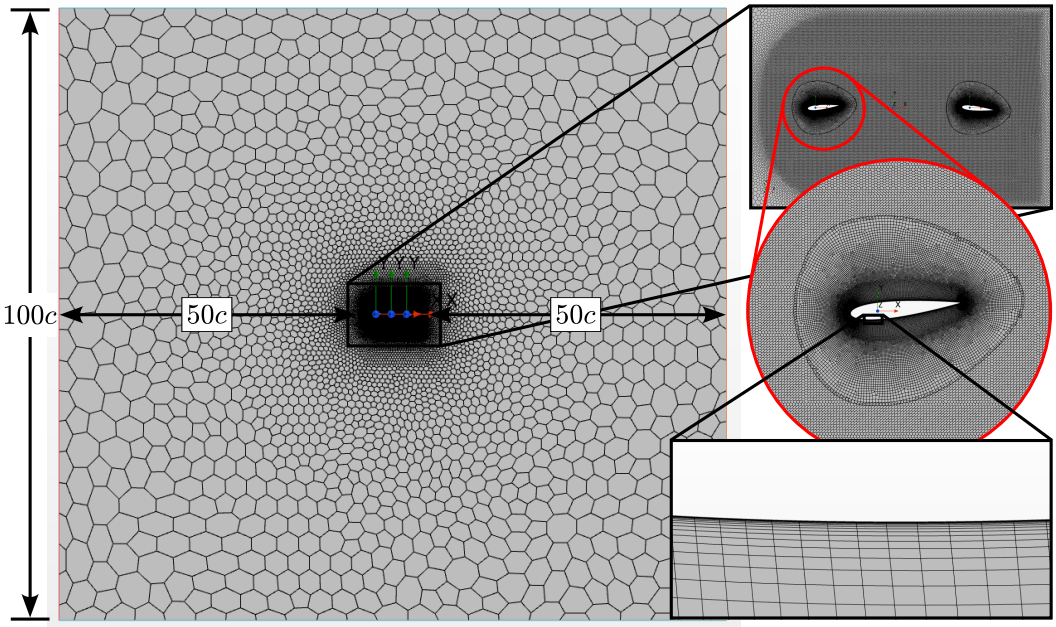



**Figure 6.** CFD domain and mesh for the FP-OFT-SAT.

*2.5. Verification*

In order to validate the mesh used in this study, the performance metrics $C_P$ and $\eta$ of a constrained OFT have been compared between three cases of varying mesh refinement and also against a reference case from Kinsey and Dumas [9]. The performance metrics of all four cases are shown in Table 2. The parameters of the constrained OFT, i.e., the reduced frequency $f^*$, the normalized heaving amplitude $H_0/c$, the pitching amplitude $\theta_0$, the normalized inter-foil spacing $L_x/c$, the normalized position of the pitch axis $x_p/c$, and the downstream foil motion phase shift relative to the upstream foil $\phi_{1-2}$ are, respectively, $f^* = 0.10$, $H_0/c = 1.00$, $\theta_0 = 70°$, $L_x/c = 7.5$, $x_p/c = 1/3$, and $\phi_{1-2} = -180°$. Though lower than the Reynolds number used in our study, i.e., Re $= 3.9 \times 10^6$, the Reynolds number used in this verification is the same as the reference case, i.e., Re = 500,000. In order to adequately compare with Kinsey and Dumas [9], the time step used in this validation

was chosen according to their same condition, such that $\Delta t^* = \min\{T^*/2000; 0.01\} = 0.005$ in the current case, and the turbulence model used is the one-equation Spalart–Allmaras model with $\tilde{\nu}/\nu = 3$ at the inlet.

**Table 2.** Results of the mesh independence study, using NACA 0015 foils, Re = 500,000, $f^* = 0.10$, $H_0/c = 1.00$, $\theta_0 = 70°$, $L_x/c = 7.5$, $x_p/c = 1/3$, and $\phi_{1-2} = -180°$.

| Case | Number of Cells | Size of Cells in Refined Zone | $C_{P_2}(\eta_2)$ | $C_{P_1}(\eta_1)$ | $C_P(\eta)$ |
|---|---|---|---|---|---|
| Coarse | 88,471 | 0.06$c$ | 0.836 (33.5) | 0.502 (20.1) | 1.339 (53.6) |
| Medium | 178,623 | 0.03$c$ | 0.839 (33.6) | 0.454 (18.2) | 1.293 (51.8) |
| Fine | 514,832 | 0.015$c$ | 0.838 (33.5) | 0.484 (19.4) | 1.321 (52.9) |
| Kinsey and Dumas [9] | 181,200 | 0.04$c$ | 0.843 (33.7) | 0.518 (20.7) | 1.360 (54.4) |

The results presented in Table 2 show that fine, medium, and coarse meshes all produce reasonably similar performance metrics against each other and against the reference case. The power coefficient of the upstream foil $C_{P_U}$ of the medium mesh is the closest to the reference case. The differences for the downstream foil (index 1) are expected and can be attributed to the more complex physics involved and the different numerical methods used in this study (overset meshes) and in the reference study [9] (sliding interfaces). It is thus expected that the wake of the upstream foil that interacts with the downstream foil may be slightly altered. Considering this, the medium mesh has been deemed to produce sufficiently accurate results and was, therefore, chosen as the final mesh for this study.

## 3. Results and Discussion

This study of the FP-OFT-SAT was aimed towards two main goals: total and partial fine-tuning of the turbine. To this end, the momentum gradient ascent (MGA) algorithm [34,35] consisting of the five steps detailed in [25] was used. In total fine-tuning, every structural parameter could change, whereby the two foils could end up having different values for each of their respective structural parameters ($I^*_{\theta_i}$, $D^*_{\theta_i}$, $k^*_{\theta_i}$, and $S^*_i$). Therefore, with the two foils having the same initial structural parameters, if the fine-tuning algorithm makes one foil have a slightly higher moment of inertia, for instance, then the change is carried out in the next iteration.

In the partial fine-tuning of the turbine, the two foils keep identical structural parameters ($I^*_{\theta_i} = I_\theta$, $D^*_{\theta_i} = D^*_\theta$, $k^*_{\theta_i} = k^*_\theta$, and $S^*_i = S^*$). The purpose of this partial fine-tuning is to reduce the potential cost and complexity of the prototype by keeping identical upstream and downstream foils.

For both the total and the partial fine-tuning processes, the turbine was studied operating under both coupled flutter and stall flutter instabilities, as well as with and without the use of gears in the design, as was the case for the FP-OFT-SA in [25]. Therefore, eight turbine configurations were fine-tuned. In this study, the MGA algorithm typically took from 10 to 20 iterations for the eight configurations analyzed. The number of iterations for the MGA algorithm to converge depends upon its internal parameters (the variables $h$ and $\gamma$ in [25]), which can be changed throughout the process, and other studies using this method may converge slower or faster, depending on the values chosen for these variables.

The base configurations used to initiate the MGA algorithm are those presented in Table 1. Comparing the performances between the single and tandem configurations using the same total arm length was thought worthwhile to indicate which configuration would offer better performances for a land footprint more or less identical when neglecting the protrusion of foils. From the high performances obtained by the FP-OFT-SA using

$L^* = 5$ in [25], we therefore analyze, in this present study, a total length of $L^*_{tot} = 5$. A ratio of $R = 0.5$ is chosen based on intuition by initially leaving out the unknown effects of positioning the arm's pivot point closer to either end. The final structural parameters and the performance metrics obtained for the total fine-tuning and the partial fine-tuning are shown in Tables 3 and 4, respectively. The values for the performance indicators are calculated as the arithmetic mean of the last two cycles if the efficiency changed by less than 0.1% between them. Otherwise, a mean value is taken over a sample of cycles, showing repeatability over time. Figure 7 illustrates the results presented in Tables 3 and 4, where error bars are traced to indicate the standard deviation (SD) of the mean taken over the sampled cycles for each case. Figures 8–11 show the normalized vorticity fields during half a cycle of the FP-OFT-SAT for all cases studied.

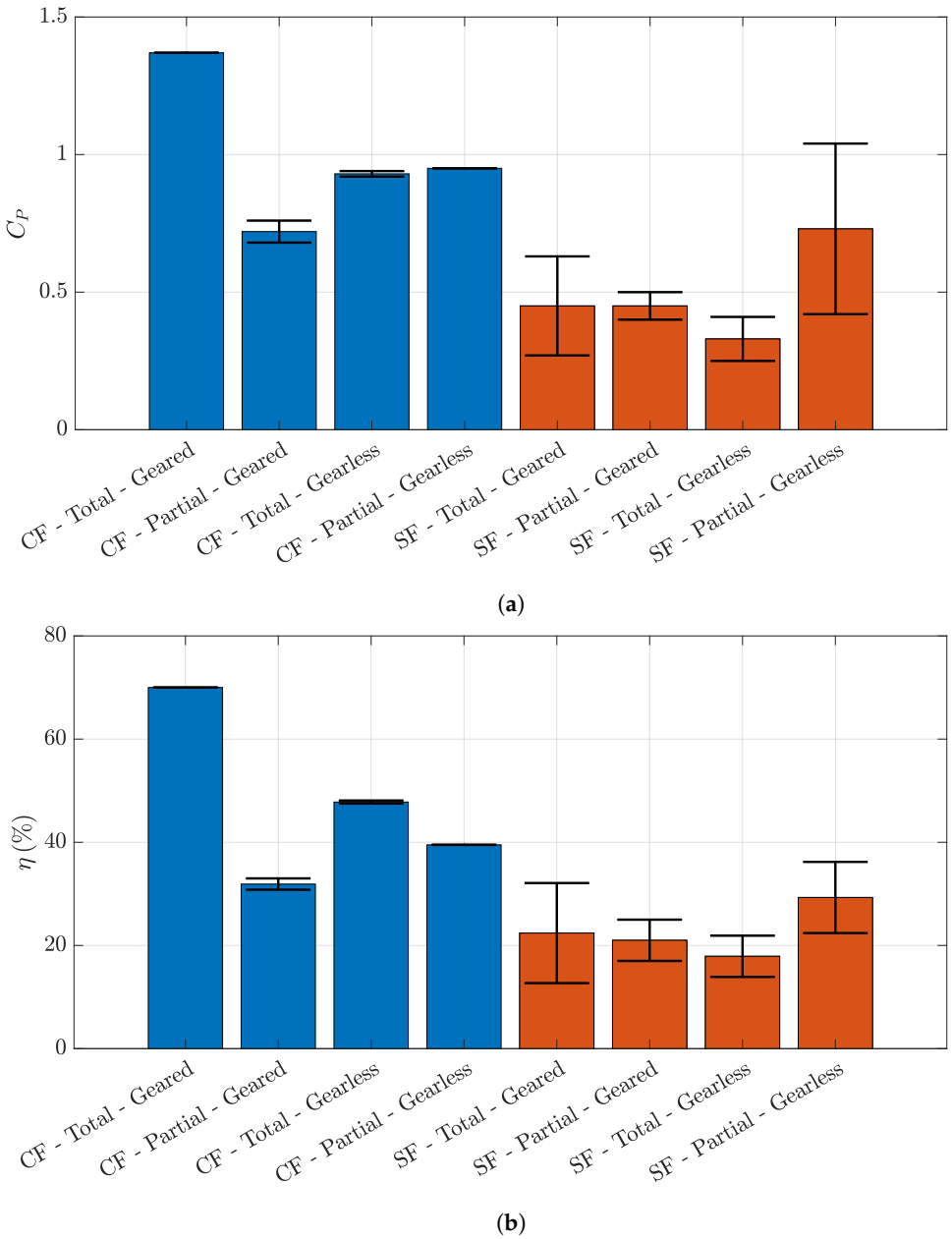
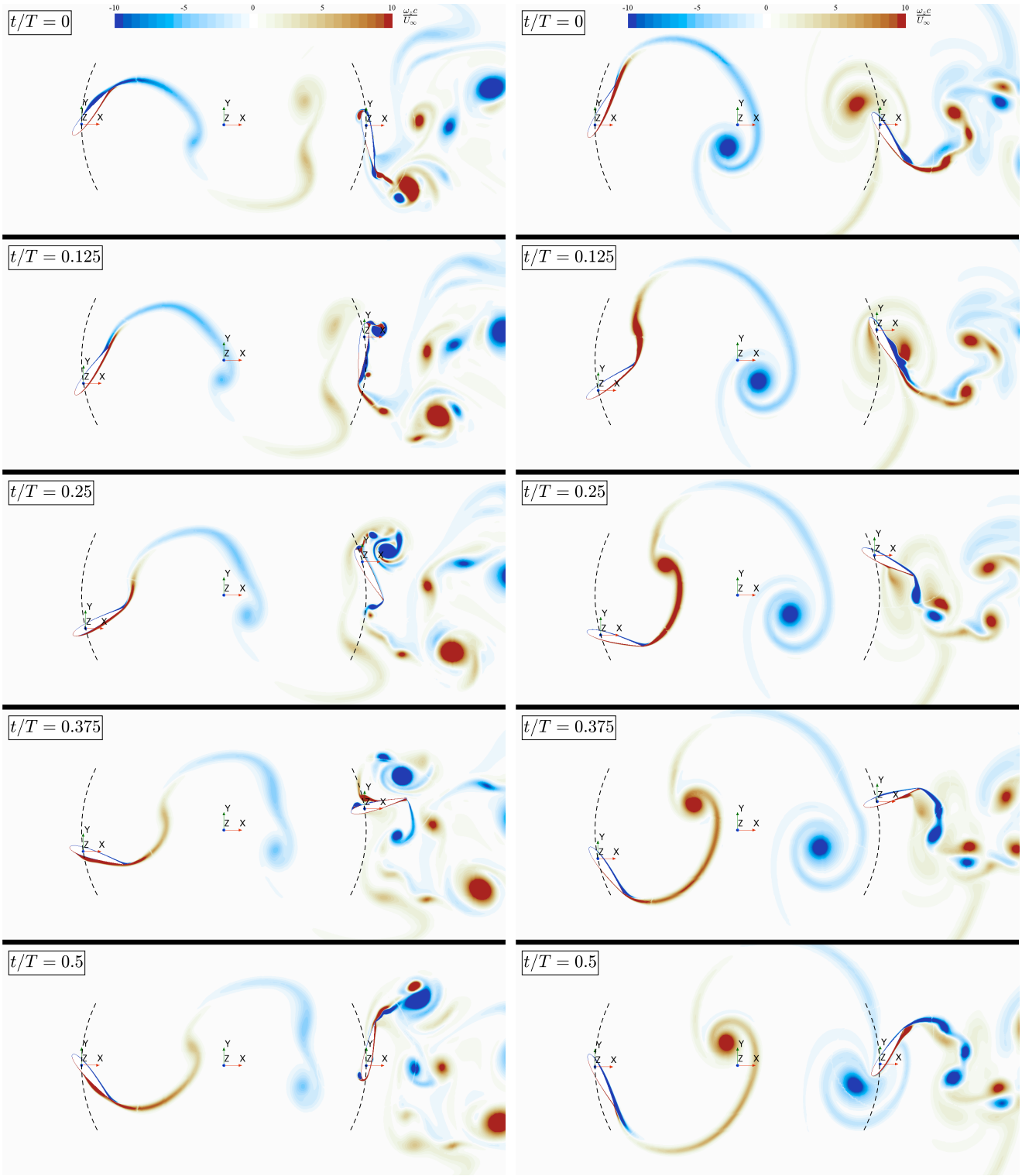
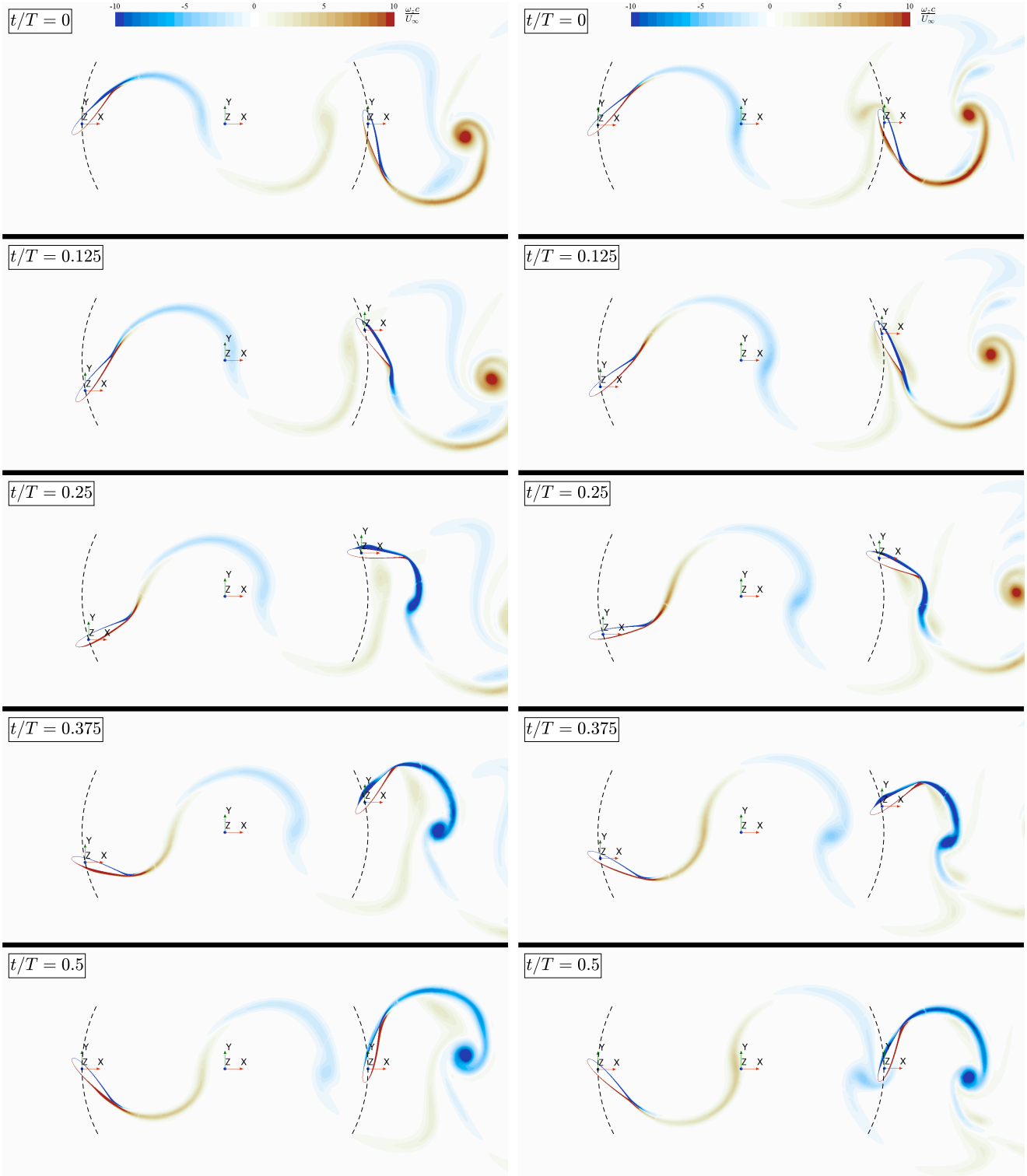



**Figure 7.** Values of (**a**) $C_P$ and (**b**) $\eta$ for the coupled flutter (CF in blue) stall flutter (SF in orange) scenarios, for total and partial fine-tuning, and for geared and gearless configurations. The error bars represent the standard deviation (SD) of the mean taken over the sampled cycles for each case.



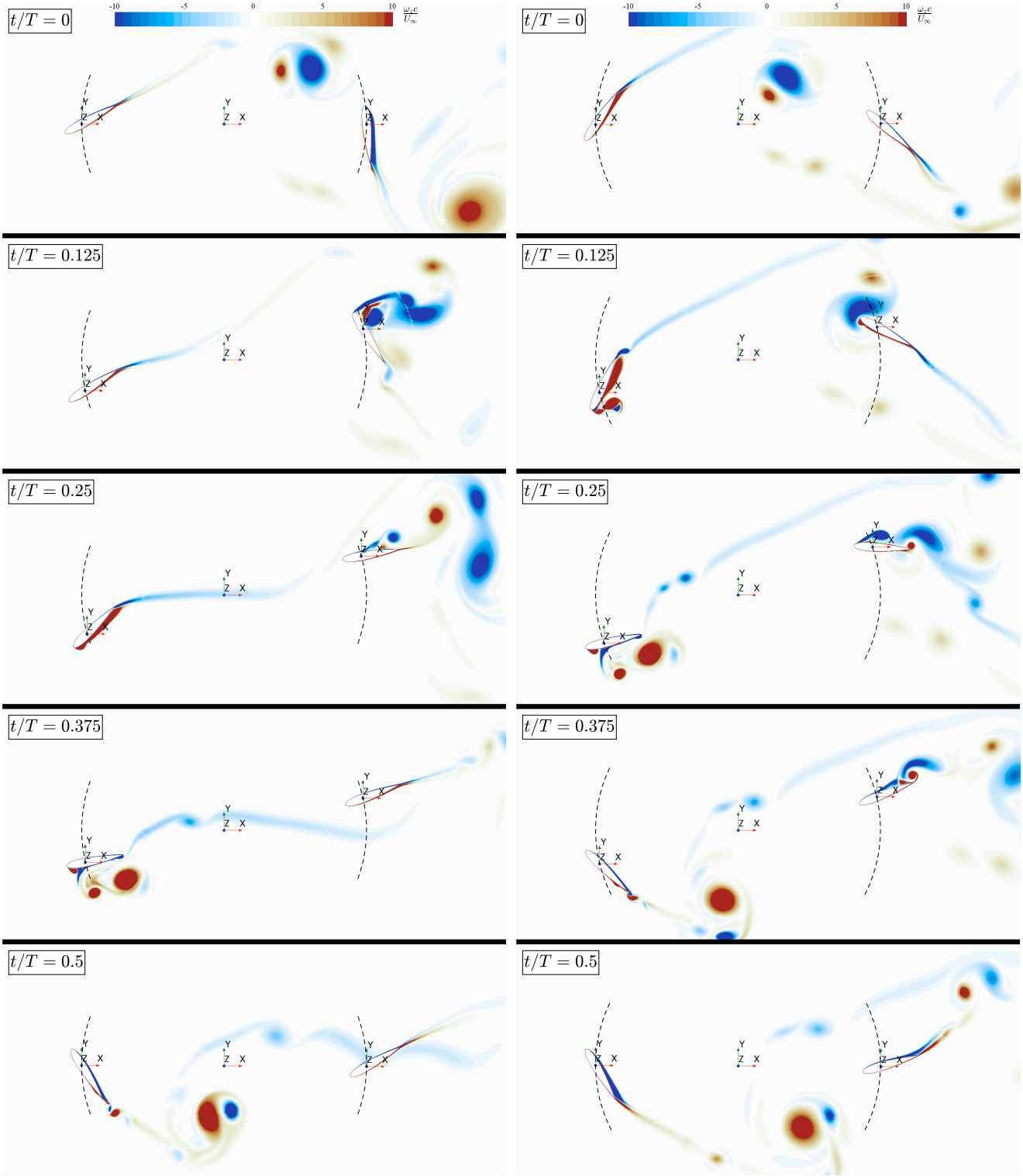

(**a**) $C_P = 0.72$, $\eta = 31.9\%$ (**b**) $C_P = 1.37$, $\eta = 70.0\%$

**Figure 8.** Normalized vorticity $\left(\omega_z^* = \frac{\omega_z c}{U_\infty}\right)$ field during half a cycle of the (**a**) partially and (**b**) totally fine-tuned FP-OFT-SAT operating under the coupled flutter instability in the geared configuration with $L_{tot}^* = 5$ and $R = 0.5$. The arched heave motions are illustrated by black dashed lines.



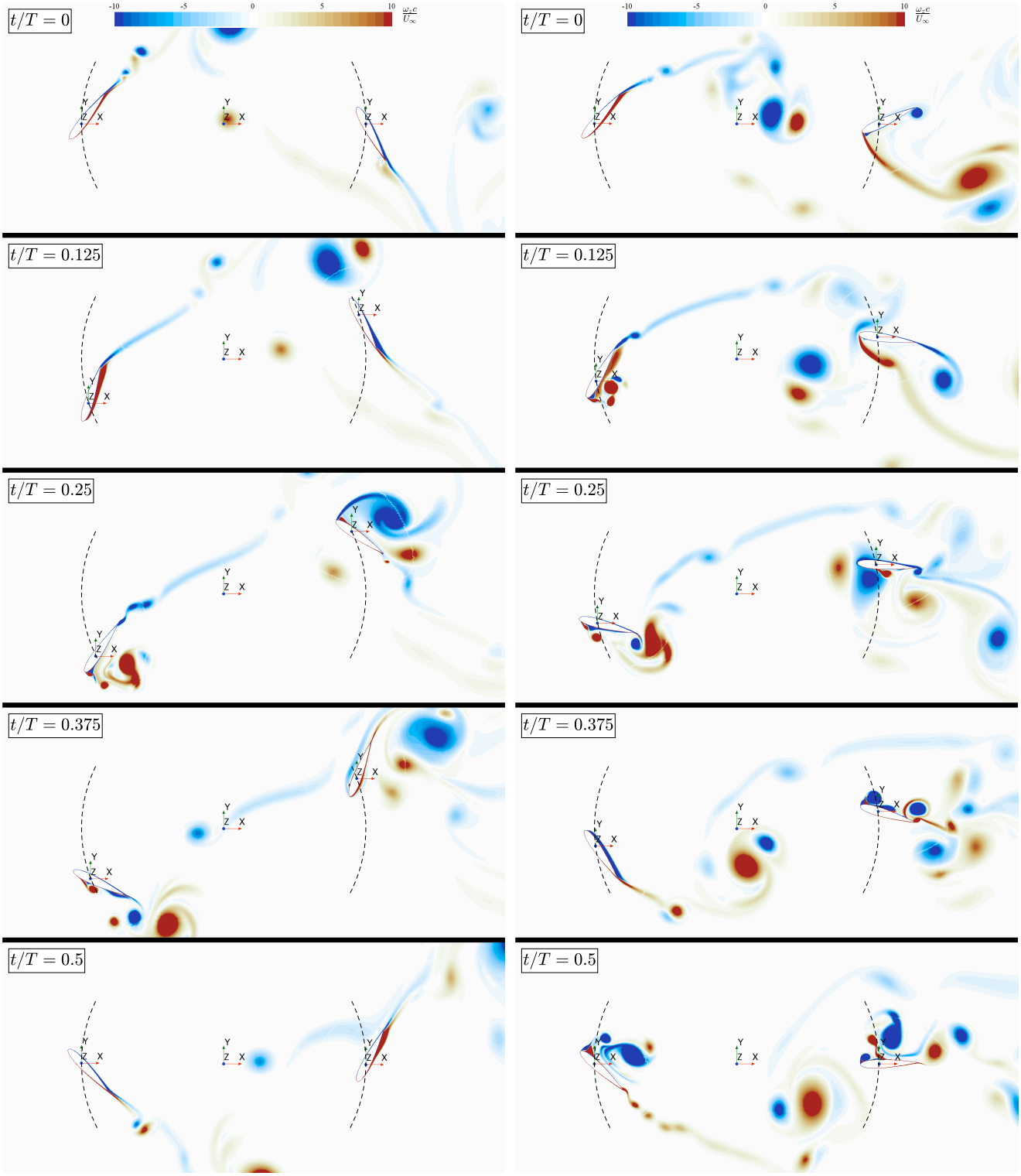

(**a**) $C_P = 0.95$, $\eta = 39.5\%$ (**b**) $C_P = 0.93$, $\eta = 47.8\%$

**Figure 9.** Normalized vorticity $\left(\omega_z^* = \frac{\omega_z c}{U_\infty}\right)$ field during half a cycle of the (**a**) partially and (**b**) totally fine-tuned FP-OFT-SAT operating under the coupled flutter instability in the gearless configuration with $L_{tot}^* = 5$ and $R = 0.5$. The arched heave motions are illustrated by black dashed lines.




(**a**) $C_P = 0.45$, $\eta = 21.0\%$ (**b**) $C_P = 0.47$, $\eta = 23.2\%$

**Figure 10.** Normalized vorticity $\left(\omega_z^* = \frac{\omega_z c}{U_\infty}\right)$ field during half a cycle of the (**a**) partially and (**b**) totally fine-tuned FP-OFT-SAT operating under the stall flutter instability in the geared configuration with $L_{tot}^* = 5$ and $R = 0.5$. The arched heave motions are illustrated by black dashed lines.




(**a**) $C_P = 0.73$, $\eta = 29.3\%$ (**b**) $C_P = 0.33$, $\eta = 17.9\%$

**Figure 11.** Normalized vorticity $\left(\omega_z^* = \frac{\omega_z c}{U_\infty}\right)$ field during half a cycle of the (**a**) partially and (**b**) totally fine-tuned FP-OFT-SAT operating under the stall flutter instability in the gearless configuration with $L_{tot}^* = 5$ and $R = 0.5$. The arched heave motions are illustrated by black dashed lines.

The MGA algorithm proved to be very effective when using coupled flutter parameters. Indeed, due to the relatively coherent structure of the flow between the two foils (see Figures 8 and 9), the downstream foil was not greatly hindered by the wake flow when its structural parameters were modified between iterations of the MGA algorithm. Because the flow maintained a similar structure between small changes in the structural parameters,

the turbine could adapt itself quickly and find its new steady-state regime. However, this was not the case when using stall flutter parameters, where the flow changed drastically between iterations of the MGA algorithm. Indeed, leading edge vortices (LEVs) shed by the upstream foil (see Figures 10 and 11) played a major role in the dynamic response of the downstream foil, causing it to be very sensitive to small changes in the structural parameters. This caused the turbine to enter longer transient periods of oscillation, and when a steady-state regime would occur, it would sometimes be much more or much less erratic than the previous iteration. This caused the MGA algorithm to advance in sawtooth patterns towards the best configurations for stall flutter cases. This highly erratic behavior can be observed through the large standard deviation (SD) values in Tables 3 and 4 and is represented by the large error bars in Figure 7. However, the stall flutter instability's superior robustness remains a key attribute. The parametric space remains large, and perhaps other parametric choices could improve the performance and regularity of stall flutter oscillations.

**Table 3.** Performance metrics for the totally fine-tuned FP-OFT-SAT with $L^*_{tot} = 5$ and $R = 0.5$ in both geared and gearless configurations using the coupled flutter and stall flutter parameters. Standard deviations (SD) are also presented, as defined in Section 2.3.

| Parameter | Coupled Flutter | | Stall Flutter | |
|---|---|---|---|---|
| | Geared | Gearless | Geared | Gearless |
| $x_P/c$ | 1/4 | 1/4 | 1/3 | 1/3 |
| $I^*_B$ | 30.237 | 123.486 | 41.670 | 38.263 |
| $D^*_\alpha$ | 9.131 | 8.396 | 21.433 | 19.070 |
| $k^*_\alpha$ | 17.948 | 169.883 | 13.914 | 15.235 |
| $I^*_{\theta_1}$ | 1.712 | 0.431 | 0.125 | 0.108 |
| $I^*_{\theta_2}$ | 1.458 | 0.397 | 0.087 | 0.103 |
| $D^*_{\theta_1}$ | 0 | 0 | 0.139 | 0.126 |
| $D^*_{\theta_2}$ | 0 | 0 | 0.128 | 0.116 |
| $k^*_{\theta_1}$ | 2.812 | 0.484 | 0.031 | 0.031 |
| $k^*_{\theta_2}$ | 2.800 | 0.635 | 0.031 | 0.031 |
| $S^*_1$ | 0.561 | 0.583 | −0.030 | −0.035 |
| $S^*_2$ | 0.683 | 0.407 | −0.030 | −0.032 |
| $C_{P_1}$ (SD) | 1.52 (0.00) | 0.77 (0.01) | 0.03 (0.17) | −0.08 (0.12) |
| $C_{P_2}$ (SD) | −0.15 (0.00) | 0.16 (0.00) | 0.42 (0.08) | 0.41 (0.08) |
| $C_P$ (SD) | 1.37 (0.00) | 0.93 (0.01) | 0.45 (0.18) | 0.33 (0.08) |
| $\eta$% (SD) | 70.0 (0.0) | 47.8 (0.3) | 22.4 (9.7) | 17.9 (4.0) |
| $T^*$ (SD) | 4.76 (0.00) | 5.08 (0.00) | 11.63 (1.14) | 10.94 (1.55) |
| $d^*$ (SD) | 1.96 (0.00) | 1.94 (0.00) | 1.90 (0.36) | 1.11 (0.35) |

In the case of the coupled flutter instability, the turbine's partial fine-tuning offers lower performance metrics than its total fine-tuning. Indeed, when the turbine is only partially fine-tuned, the values of the structural parameters are limited by the constraint of being equal between two foils, which hinders the possible gains in performance metrics. When every parameter is free to change its value to appropriately follow the gradient of the functions of $\eta$ and $C_P$, the MGA algorithm can then better follow said gradient to higher values of the performance metrics. For instance, for the best case reported in Table 3 for total fine-tuning, the highest relative difference of 21.7% is observed between two static imbalances, indicating relatively small modifications to be made on each foil.

As is indicated in Table 3, the best configuration found in this study is the fine-tuned geared FP-OFT-SAT operating under the coupled flutter instability, achieving a power coefficient of $C_{P_{tot}} = 1.37$, which is minimally 45% superior to the other configurations. Figure 12 shows the contribution of both foils to the overall power coefficient.

**Table 4.** Performance metrics for the partially fine-tuned FP-OFT-SAT with $L^*_{tot} = 5$ and $R = 0.5$ in both geared and gearless configurations using coupled flutter and stall flutter parameters. Standard deviations (SD) are also presented, as defined in Section 2.3.

| Parameter | Coupled Flutter | | Stall Flutter | |
|---|---|---|---|---|
| | Geared | Gearless | Geared | Gearless |
| $x_P/c$ | 1/4 | 1/4 | 1/3 | 1/3 |
| $I^*_B$ | 22.488 | 122.923 | 41.515 | 37.445 |
| $D^*_\alpha$ | 10.008 | 7.492 | 19.945 | 18.510 |
| $k^*_\alpha$ | 21.668 | 158.817 | 14.836 | 13.177 |
| $I^*_{\theta_i}$ | 2.474 | 0.397 | 0.088 | 0.084 |
| $D^*_{\theta_i}$ | 0 | 0 | 0.124 | 0.106 |
| $k^*_{\theta_i}$ | 3.024 | 0.495 | 0.031 | 0.031 |
| $S^*_i$ | 0.512 | 0.411 | −0.029 | −0.028 |
| $C_{P_1}$ (SD) | 0.31 (0.03) | 0.61 (0.00) | −0.07 (0.09) | 0.09 (0.20) |
| $C_{P_2}$ (SD) | 0.41 (0.01) | 0.34 (0.00) | 0.52 (0.10) | 0.64 (0.16) |
| $C_P$ (SD) | 0.72 (0.04) | 0.95 (0.00) | 0.45 (0.05) | 0.73 (0.31) |
| $\eta$% (SD) | 31.9 (1.1) | 39.5 (0.0) | 21.0 (4.0) | 29.3 (6.9) |
| $T^*$ (SD) | 5.84 (0.08) | 5.30 (0.00) | 12.07 (1.53) | 11.00 (1.24) |
| $d^*$ (SD) | 2.27 (0.05) | 2.41 (0.00) | 2.15 (0.20) | 2.38 (0.59) |

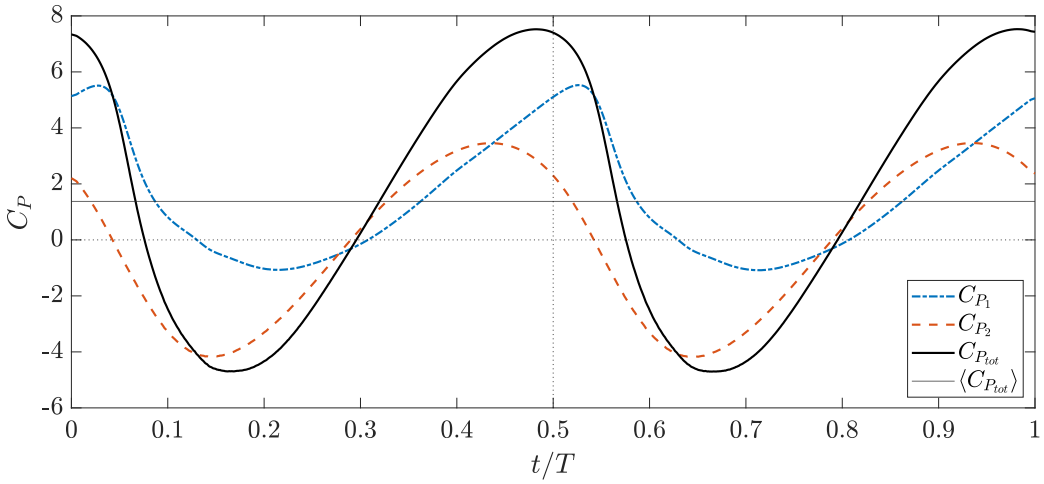



**Figure 12.** Instantaneous power coefficient ($C_{P_{tot}} = C_{P_1} + C_{P_2}$) during a complete cycle of the totally fine-tuned FP-OFT-SAT operating under the coupled flutter instability in the geared configuration and $L^*_{tot} = 5$ and $R = 0.5$. The solid gray line indicates the mean value of $\langle C_{P_{tot}} \rangle = 1.37$ in the cycle.

Surprisingly, the upstream foil has a mean value of $C_{P_2} = -0.15$ in a cycle, which corresponds to a small power consumption. However, the motion of the upstream foil is the driving factor for the high power coefficient of the downstream foil of $C_{P_1} = 1.52$, which provides an overall value of $C_{P_{tot}} = 1.37$. The reasons are two-fold: firstly, the vortices shed at the trailing edge of the upstream foil come close to the leading edge of the downstream foil such that the induced velocity by the vortices increases the dynamic pressure applied on the downstream foil, increasing its vertical force component and, in turn, its power coefficient. This was reported as "Case v1" by Kinsey and Dumas [9], who classified the different interactions of the downstream foil and the wake vortices for the tandem constrained OFT. Secondly, when the vortices begin passing around the downstream foil, they travel along its upper surface, as can be seen in Figure 8b. The presence of low pressure associated with these vortices enhances the suction on the upper surface of the foil. In these two instances, the instantaneous power coefficient of the downstream foil is thus greatly

enhanced by having an overall higher vertical force component, yielding instantaneous values of the power coefficient slightly above $C_{P_1} \approx 5.5$.

The $C_P$ of the FP-OFT-SAT is slightly inferior to that of the FP-OFT-SA reported in [25] for the same overall land footprint of $L^*_{tot} = 5$, having a relative decrease of 12.7% from 1.57 for the FP-OFT-SA to 1.37 for the FP-OFT-SAT. However, the efficiency of the FP-OFT-SAT has a relative increase of 28.0% from 54.7% for the FP-OFT-SA to 70.0% for the FP-OFT-SAT. As was argued by Kinsey and Dumas [9], such a high value of efficiency stems from the fact that turbulence and viscous mixing can transfer flow momentum from the free stream above and below the turbine into the inter-foil wake. Therefore, efficiency values over the theoretical inviscid Betz limit for tandem configurations of 64% [36] can be achieved, such as in the present study. Since the power coefficient is the indicator of the turbine's capacity to extract power, the higher value of $C_P$ of the FP-OFT-SA from [25] indicates that the FP-OFT-SA is better suited for the same land footprint of $L^*_{tot} = 5$ than the FP-OFT-SAT, even though the latter offers a higher efficiency value.

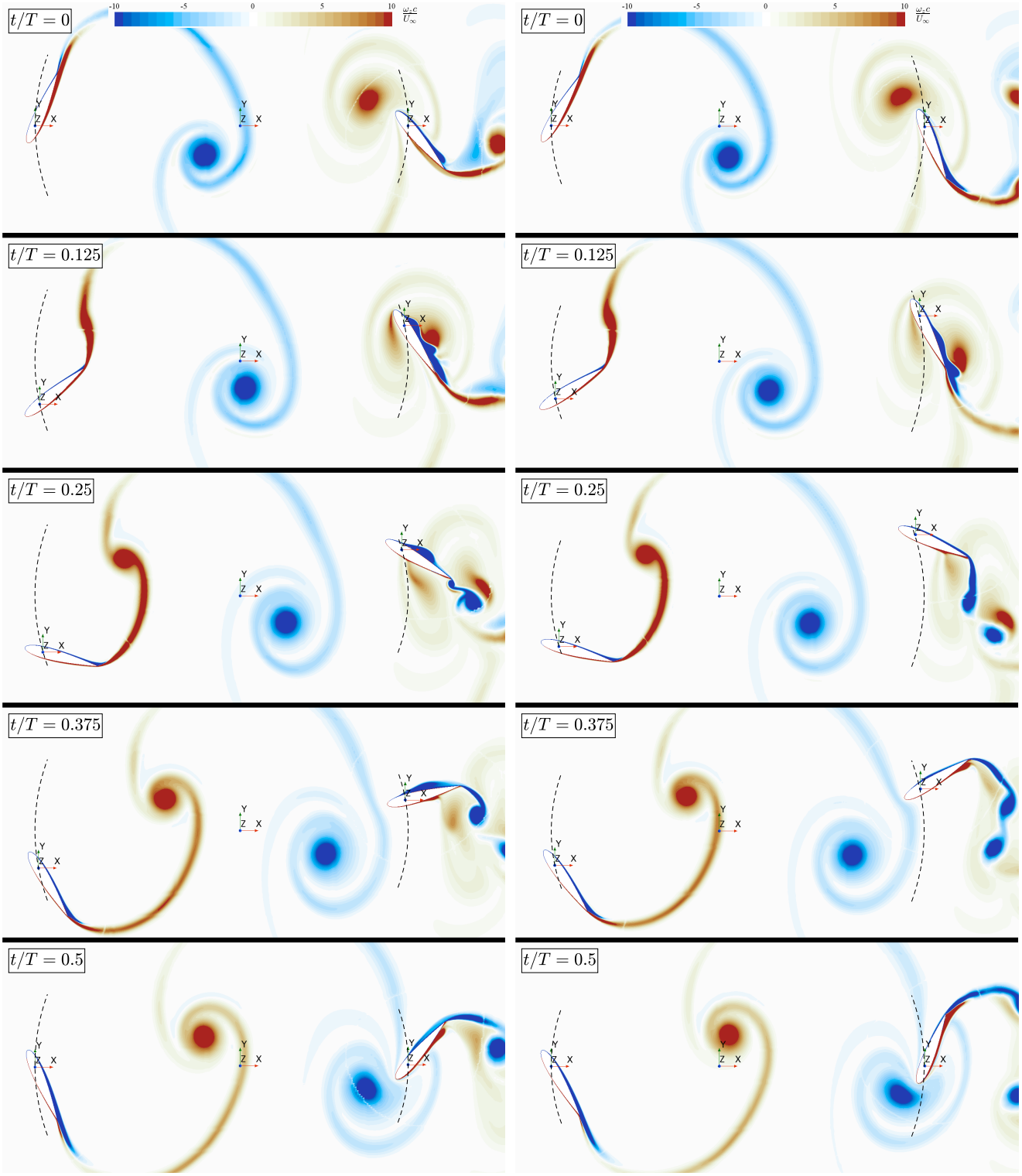
### *3.1. Effects of the Position of the Arm's Pivot Point*

In this section, we evaluate the effects of varying the position of the pivot point $Q$. To do so, the value of the ratio $R$ is varied slightly while ensuring $L^*_{tot} = 5$. Only the best configuration previously found, i.e., the fine-tuned geared configuration operating under the coupled flutter instability in Table 3, is used in this section.

Firstly, the values of the structural parameters are kept equal to those of Table 3. The goal here is to assess the sensitivity of the turbine to its pivot's precise placement. Values of $R = 0.45$ and $R = 0.55$ are tested using $L^*_{tot} = 5$ to determine the effects of small displacement in either downstream or upstream directions along the arm. Then, using Equations (11)–(13), the heave structural parameters ($I^*_B$, $D^*_\alpha$, and $k^*_\alpha$) are varied for both the $R = 0.45$ and $R = 0.55$ cases. The corresponding performance metrics for these four new cases are presented in Table 5, and Figures 13 and 14 show half a cycle of all cases.

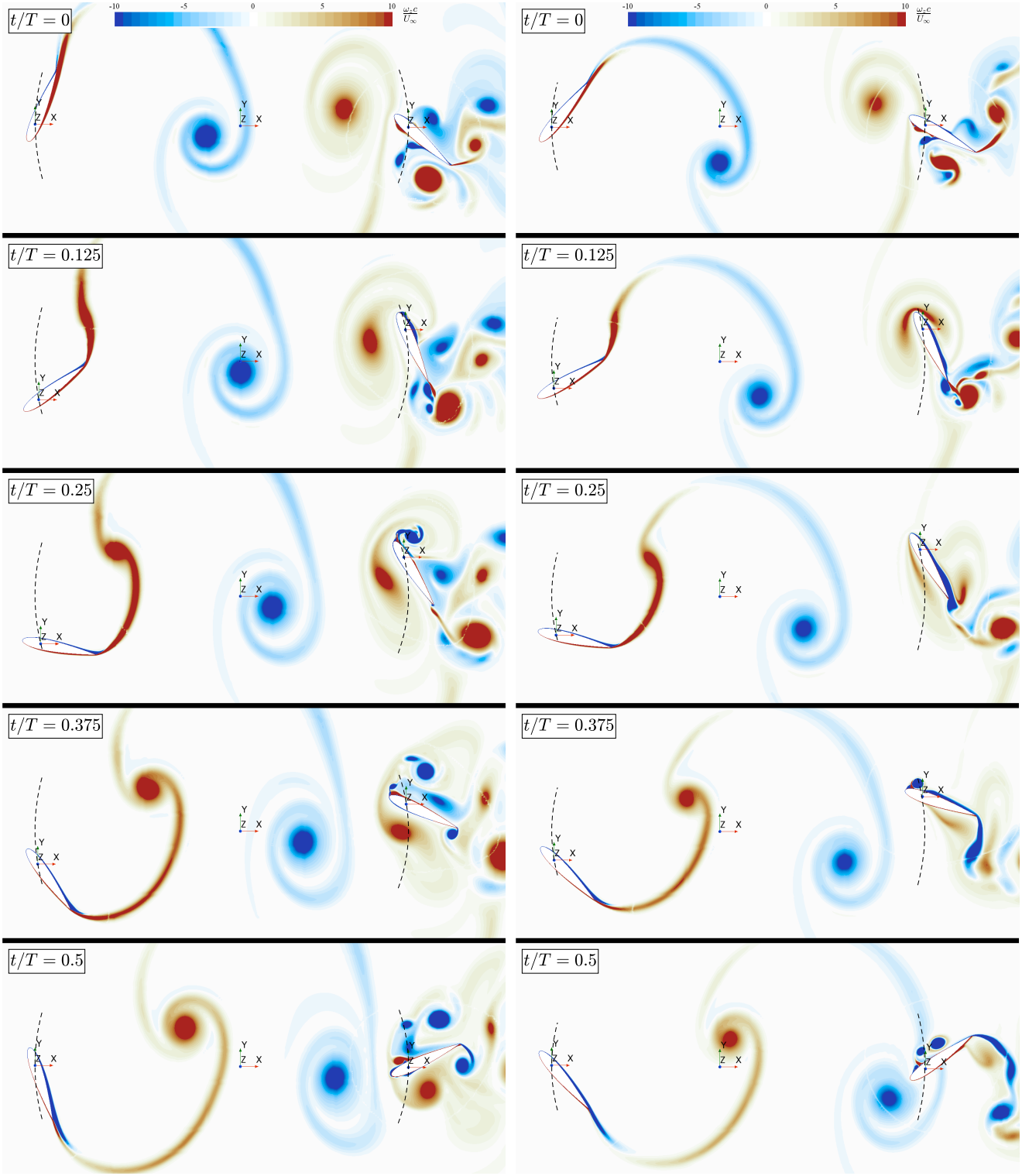
Interestingly, the case using constant heave values and $R = 0.55$ offers better performance metrics than the initial $R = 0.5$ case. Indeed, by shifting the pivot point $Q$ slightly towards the upstream foil while keeping all structural parameters constant, the trailing edge vortices shed by the upstream foil reach the downstream foil such that the suction on the upper surface of the downstream foil is slightly better timed, compared to the $R = 0.5$ case. Indeed, Figure 15 shows that the suction on the upper surface of the downstream foil makes it now reach instantaneous values of $C_{P_1} \approx 6.7$, providing a cycle average of $C_{P_1} = 1.73$. With the upstream foil still in power consumption mode, with $C_{P_2} = -0.27$, a new overall power coefficient of $C_{P_{tot}} = 1.46$ is found, while the efficiency value now reaches 74.9%. This results in relative increases of 6.6% and 7.0% for the power coefficient and the efficiency, respectively, showing adequate justification for shifting the pivot point $Q$ to adjust the FP-OFT-SAT for additional power extraction. Further investigation into this idea is, however, beyond the scope of this study.

In the two cases in which the heave parameters are scaled, the performances obtained are much lower than those of the base case of $R = 0.5$. Figure 14 shows how the inter-foil wake vortices are now approaching the downstream foil such that a negative interaction arises between them. The downstream foil is being greatly hindered, and the whole turbine has much difficulty in reaching a steady-state regime, behaving with large variations in its performance metrics. Therefore, when changed according to Equations (11)–(13), the turbine's heave parameters seem to necessitate a higher degree of fine-tuning when the pivot is slightly moved along the arm. Again, further investigation into this fine-tuning, especially at other values of $R$, is out of the scope of this study and is left for future works.




(**a**) $C_P = 1.26$, $\eta = 60.2\%$ (**b**) $C_P = 1.46$, $\eta = 74.9\%$

**Figure 13.** Normalized vorticity $\left(\omega_z^* = \frac{\omega_z c}{U_\infty}\right)$ field during half a cycle of the totally fine-tuned FP-OFT-SAT operating under the coupled flutter instability in the geared configuration with $L_{tot}^* = 5$ and (**a**) $R = 0.45$ and (**b**) $R = 0.55$; the values of the structural parameters are those of the geared FP-OFT-SAT operating under the coupled flutter instability of Table 3. The arched heave motions are illustrated by black dashed lines.




(**a**) $C_P = 0.79$, $\eta = 35.3\%$ (**b**) $C_P = 0.63$, $\eta = 32.8\%$

**Figure 14.** Normalized vorticity $\left(\omega_z^* = \frac{\omega_z c}{U_\infty}\right)$ field during half a cycle of the totally fine-tuned FP-OFT-SAT operating under the coupled flutter instability in the geared configuration with $L_{tot}^* = 5$ and (**a**) $R = 0.45$ and (**b**) $R = 0.55$; the values of the structural parameters are those of the geared FP-OFT-SAT operating under the coupled flutter instability of Table 3 with scaled values for $I_B^*$, $D_\alpha^*$, and $k_\alpha^*$. The arched heave motions are illustrated by black dashed lines.

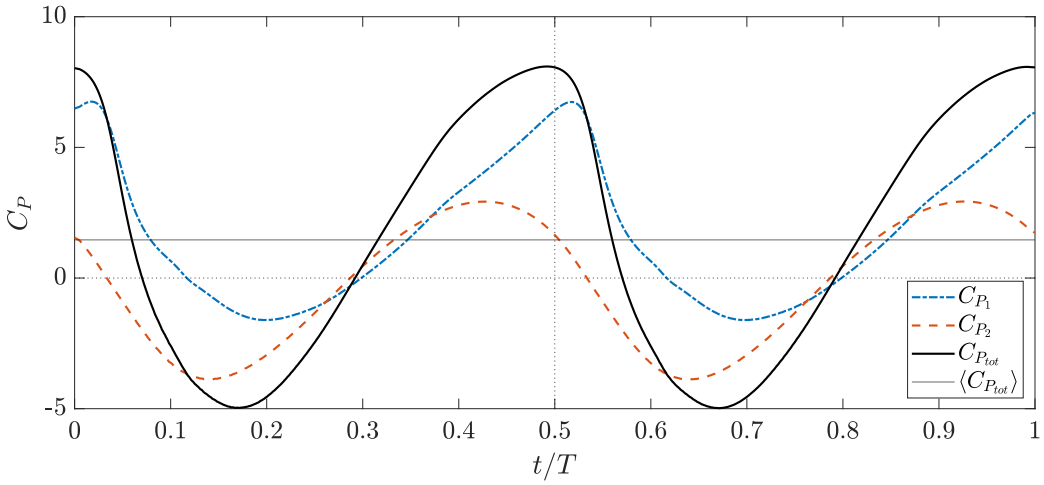


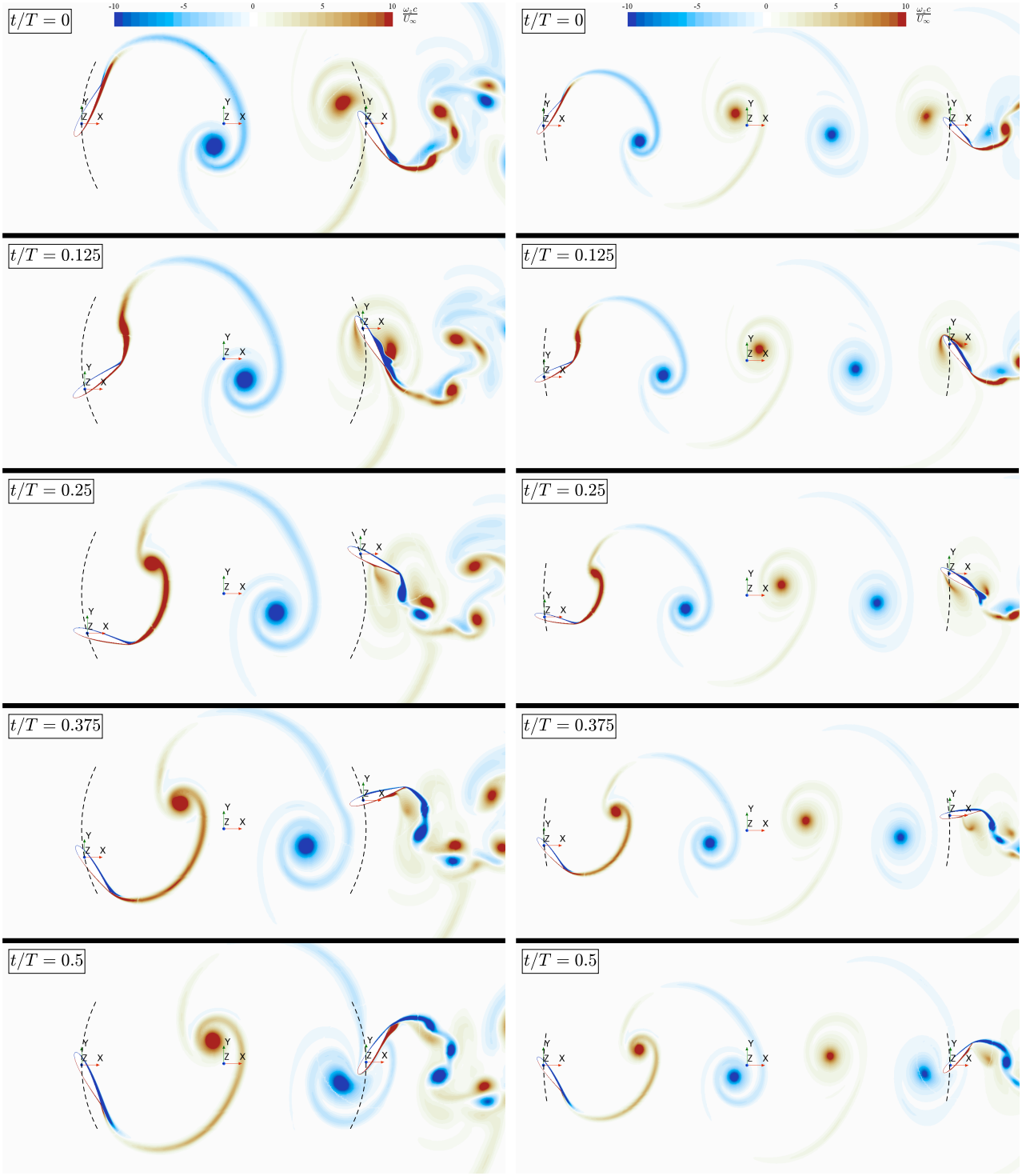

**Figure 15.** Instantaneous power coefficient ($C_{P_{tot}} = C_{P_1} + C_{P_2}$) during a complete cycle of the totally fine-tuned FP-OFT-SAT operating under the coupled flutter instability in the geared configuration and $L^*_{tot} = 5$ and $R = 0.55$. The solid gray line indicates the mean value of $C_{P_{tot}} = 1.46$ in the cycle.

**Table 5.** Performance metrics for the optimal FP-OFT-SAT using gears and operating under the coupled flutter instability with $L^*_{tot} = 5$ and $R = 0.45$ and $R = 0.55$; the values of the structural parameters are those of the geared FP-OFT-SAT operating under the coupled flutter instability of Table 3. Standard deviations (SD) are also presented, as defined in Section 2.3.

| **Parameter** | **Initial** | **Constant Heave Parameters** | | **Scaled Heave Parameters** | |
|---|---|---|---|---|---|
| | $R = 0.50$ | $R = 0.45$ | $R = 0.55$ | $R = 0.45$ | $R = 0.55$ |
| $I^*_B$ | 30.237 | 30.237 | 30.237 | 20.359 | 20.359 |
| $D^*_\alpha$ | 9.131 | 9.131 | 9.131 | 6.148 | 6.148 |
| $k^*_\alpha$ | 17.948 | 17.948 | 17.948 | 12.085 | 12.085 |
| $I^*_{\theta_1}$ | 1.712 | 1.712 | 1.712 | 1.712 | 1.712 |
| $I^*_{\theta_2}$ | 1.458 | 1.458 | 1.458 | 1.458 | 1.458 |
| $D^*_{\theta_1}$ | 0 | 0 | 0 | 0 | 0 |
| $D^*_{\theta_2}$ | 0 | 0 | 0 | 0 | 0 |
| $k^*_{\theta_1}$ | 2.812 | 2.812 | 2.812 | 2.812 | 2.812 |
| $k^*_{\theta_2}$ | 2.800 | 2.800 | 2.800 | 2.800 | 2.800 |
| $S^*_1$ | 0.561 | 0.561 | 0.561 | 0.561 | 0.561 |
| $S^*_2$ | 0.683 | 0.683 | 0.683 | 0.683 | 0.683 |
| $C_{P_1}$ (SD) | 1.52 (0.00) | 1.26 (0.00) | 1.73 (0.00) | 0.56 (0.22) | 0.71 (0.37) |
| $C_{P_2}$ (SD) | −0.15 (0.00) | 0.00 (0.00) | −0.27 (0.00) | 0.23 (0.14) | −0.08 (0.12) |
| $C_P$ (SD) | 1.37 (0.00) | 1.26 (0.00) | 1.46 (0.00) | 0.79 (0.29) | 0.63 (0.42) |
| $\eta$% (SD) | 70.0 (0.0) | 60.2 (0.0) | 74.9 (0.0) | 35.3 (11.0) | 32.8 (21.7) |
| $T^*$ (SD) | 4.76 (0.00) | 4.73 (0.00) | 4.78 (0.00) | 4.67 (0.25) | 4.68 (0.18) |
| $d^*$ (SD) | 1.96 (0.00) | 2.10 (0.00) | 1.95 (0.00) | 2.19 (0.15) | 1.97 (0.67) |

### *3.2. Effects of the Length of the Arm*

In this section, a new length is studied to observe the response of the fine-tuned FP-OFT-SAT. A longer length of $L^*_{tot} = 10$ is chosen, with the pivot point $Q$ still at the middle point of the arm ($R = 0.5$). In this new case, all heave parameters ($I^*_B$, $D^*_\alpha$, and $k^*_\alpha$) are scaled to this new length according to Equations (11)–(13) to ensure that a similar dynamic response is achieved. The structural parameters and the performance metrics of this new case are shown and compared to the initial $L^*_{tot} = 5$ case in Table 6 whereas the vorticity fields are compared in Figure 16.




(**a**) $C_P = 1.37$, $\eta = 70.0\%$ (**b**) $C_P = 0.67$, $\eta = 46.2\%$

**Figure 16.** Normalized vorticity $\left(\omega_z^* = \frac{\omega_z c}{U_\infty}\right)$ field during half a cycle for $R = 0.5$ and (**a**) $L_{tot}^* = 5$ and (**b**) $L_{tot}^* = 10$. The arched heave motions are illustrated by black dashed lines.

The results show that scaling the heave parameters according to Equations (11)–(13) does indeed yield acceptable performances. Furthermore, even if the performance metrics are lower than those of the initial fine-tuned $L_{tot}^* = 5$ case, they still offer a steady-state regime with relatively low variations in amplitudes, showing good functionality and stability when scaling is appropriately performed, as was the case for the FP-OFT-SA

in [25]. Another aspect through which good performances can be viewed is the effective heave stiffness. The effective heave stiffness is presented in [25] and written as follows:

$$\lambda_h^* = k_h^* - (2\pi f^*)^2 m_h^*, \tag{20}$$

proving to be a useful parameter in order to maintain similar performance metrics for different values of the structural parameters for the FP-OFT-SA. In the tandem case, the fine-tuned configuration using $L_{tot}^* = 5$ has a value of $\lambda_h^* \approx -2.8$, and this value remains unchanged when scaling the structural parameters for the $L_{tot}^* = 10$ case. However, while the performance metrics are still good, it may prove necessary to fine-tune the FP-OFT-SAT for each new length of interest in order to achieve as high performances as those of the fine-tuned $L_{tot}^* = 5$ case. In such cases of considering new lengths, performing the MGA algorithm using the scaled values as an initial configuration should reduce the number of iterations required to reach better performance at this new length.

**Table 6.** Performance metrics for the FP-OFT-SAT using gears and operating under the coupled flutter instability with $L_{tot}^* = 5$ and 10 and $R = 0.5$. Standard deviations (SD) are also presented, as defined in Section 2.3.

| Parameter | $L_{tot}^* = 5$ | $L_{tot}^* = 10$ |
|---|---|---|
| $I_B^*$ | 30.237 | 120.947 |
| $D_\alpha^*$ | 9.131 | 36.524 |
| $k_\alpha^*$ | 17.948 | 71.791 |
| $I_{\theta_1}^*$ | 1.712 | 1.712 |
| $I_{\theta_2}^*$ | 1.458 | 1.458 |
| $D_{\theta_1}^*$ | 0 | 0 |
| $D_{\theta_2}^*$ | 0 | 0 |
| $k_{\theta_1}^*$ | 2.812 | 2.812 |
| $k_{\theta_2}^*$ | 2.800 | 2.800 |
| $S_1^*$ | 0.561 | 0.561 |
| $S_2^*$ | 0.683 | 0.683 |
| $C_{P_1}$ (SD) | 1.52 (0.00) | 0.89 (0.08) |
| $C_{P_2}$ (SD) | −0.15 (0.00) | −0.22 (0.02) |
| $C_P$ (SD) | 1.37 (0.00) | 0.67 (0.08) |
| $\eta$% (SD) | 70.0 (0.0) | 46.2 (4.2) |
| $T^*$ (SD) | 4.76 (0.00) | 4.73 (0.03) |
| $d^*$ (SD) | 1.96 (0.00) | 1.45 (0.06) |

## 4. Conclusions

This paper constitutes Part 2 of our investigation of a fully passive oscillating foil turbine on a swinging arm, with Part 1 being our recent paper in *Energies* [25]. The main goal of this study was to assess the stability and the performance of this concept in a tandem configuration, based on the premise that an inherent difficulty would lie in the interaction of the downstream foil and the highly rotational wake of the upstream foil. To evaluate this new turbine concept, four configurations were fine-tuned using a momentum gradient ascent (MGA) algorithm: with and without the use of gears to alleviate a resisting torque on the arm and relying either on the coupled flutter or stall flutter instability to produce steady-state oscillations. All of these configurations were studied through 2D URANS CFD simulations using a normalized total length of the arm of $L_{tot} = 5c$. We concede, of course, that other lengths of the arm should be investigated to observe the effects on the structural parameters and that three-dimensional effects can significantly hinder the turbine's predicted performances.

The results show that total fine-tuning of the FP-OFT-SAT offers greater performance metrics than partial fine-tuning (the same parameters for both foils). From total fine-tuning, the geared configuration operating under the coupled flutter instability proved to offer, by far, the best performance. In addition, the FP-OFT-SAT was found to be quite sensitive and less regular when relying on the stall flutter instability, which we recommend discarding for this turbine concept. As for the coupled flutter instability, the MGA algorithm made the FP-OFT-SAT adapt such that it could use the rotational wake of the upstream foil to produce higher dynamic pressure on the downstream foil as the vortices advance towards it while also increasing suction on the upper surface of the downstream foil as the vortices travel along it. These two interaction mechanisms were found to be the driving factors for good power extraction and high-efficiency values. Indeed, even if the power coefficient is slightly inferior to the turbine undergoing linear heaving kinematics or to the FP-OFT-SA of the same land footprint, the overall efficiency is found to be significantly higher in the case of the tandem configuration, reaching an efficiency value of 70%. Thereafter, investigations on the effects of the placement of the pivot point of the arm and of the length of the arm have also shown how the turbine can respond positively to these new configurations, with one configuration reaching an efficiency value near 75%.

For future works, further investigation into the gearless configuration should be considered. Indeed, while the geared configuration produces significantly better efficiencies, the mechanical complexity of such a device and its potential maintenance requirements are significant drawbacks. Also, investigations into the use of two FP-OFT-SAs, where one is upstream of the other and uses the same footprint as the tandem configuration, would provide great insight. This would allow for a variable phase shift between the motions of the two foils and for the investigation of the global phase shift of the system. It would, therefore, show if two independent swinging arms could perform better than a single tandem arm.

It would also be worthwhile to see the effect of a perturbed inflow on the tandem configuration. Indeed, in the present simulations, the inflow consisted of a clean and uniform velocity. It would be interesting to verify how robust the turbine is when both foils experience highly perturbed flows. This would also shed light on the practicality of an array of FP-OFT-SATs.

Of course, three-dimensional studies of the tandem turbine would also be greatly appropriate to ensure that the good performances obtained in 2D are still viable in 3D. Indeed, with 3D flows, the vortices in the wake of the upstream turbine may become unstable before reaching the downstream foil, consequently lowering or even hindering their impact on the downstream foil. The finite span of the foils would introduce tip losses, which might reduce performance. The use of end plates might be advantageous. This 3D investigation would also serve as a better prediction for future experimental studies.

**Author Contributions:** Conceptualization, D.C., M.O. and G.D.; Methodology, D.C.; Validation, D.C.; Formal analysis, D.C., M.O. and G.D.; Investigation, D.C.; Resources, G.D.; Data curation, D.C.; Writing—original draft preparation, D.C.; Writing—review and editing, M.O. and G.D.; Visualization, D.C.; Supervision, M.O. and G.D.; Funding acquisition, G.D. and M.O. All authors have read and agreed to the published version of the manuscript.

**Funding:** Financial support from the Natural Sciences and Engineering Research Council of Canada (NSERC Discovery Grant No. RGPIN-2018-04527) and the Fonds de Recherche du Québec – Nature et Technologies (FRQNT Samuel-De-Champlain No. 301088) is gratefully acknowledged. The computational resources used for this study were provided by the Digital Research Alliance of Canada and Calcul Québec.

**Data Availability Statement:** The original contributions presented in this study are included in the article. Further inquiries can be directed to the corresponding author.

**Acknowledgments:** The authors would like to acknowledge all members of the LMFN CFD Laboratory for their insightful comments over the course of this study.

**Conflicts of Interest:** The authors declare no conflicts of interest. The funders had no role in the design of the study; in the collection, analyses, or interpretation of data; in the writing of the manuscript; or in the decision to publish the results.

## Abbreviations

The following abbreviations are used in this manuscript:

| | |
|---|---|
| CFD | Computational fluid dynamics |
| FP-OFT | Fully passive oscillating foil turbine |
| FP-OFT-SA | Fully passive oscillating foil turbine on a swinging arm |
| FP-OFT-SAT | Fully passive oscillating foil turbine on a swinging arm in a tandem configuration |
| LEV | Leading-edge vortex |
| OFT | Oscillating foil turbine |
| SP-OFT | Semi-passive oscillating foil turbine |
| URANS | Unsteady Reynolds-averaged Navier–Stokes |

## References

1. Liu, Z.; Qu, H.; Song, X.; Chen, Z. A state-of-the-art review on energy-harvesting performance of the flapping hydrofoil with influential parameters. *Renew. Energy* **2025**, *245*, 122849. [CrossRef]
2. McKinney, W.; DeLaurier, J. Wingmill: An Oscillating-Wing Windmill. *J. Energy* **1981**, *5*, 109–115. [CrossRef]
3. Kinsey, T.; Dumas, G.; Lalande, G.; Ruel, J.; Méhut, A.; Viarouge, P.; Lemay, J.; Jean, Y. Prototype testing of a hydrokinetic turbine based on oscillating hydrofoils. *Renew. Energy* **2011**, *36*, 1710–1718. [CrossRef]
4. Young, J.; Lai, J.C.; Platzer, M.F. A review of progress and challenges in flapping foil power generation. *Prog. Aerosp. Sci.* **2014**, *67*, 2–28. [CrossRef]
5. Young, J.; Lai, J.; Platzer, M. Flapping foil power generation: Review and potential in pico-hydro application. In Proceedings of the 2015 International Conference on Sustainable Energy Engineering and Application (ICSEEA), Bandung, Indonesia, 5–7 October 2015; pp. 95–100. [CrossRef]
6. Xiao, Q.; Zhu, Q. A review on flow energy harvesters based on flapping foils. *J. Fluids Struct.* **2014**, *46*, 174–191. [CrossRef]
7. Wu, X.; Zhang, X.; Tian, X.; Li, X.; Lu, W. A review on fluid dynamics of flapping foils. *Ocean. Eng.* **2020**, *195*, 106712. [CrossRef]
8. Ashraf, M.A.; Young, J.; Lai, J.C.S.; Platzer, M.F. Numerical Analysis of an Oscillating-Wing Wind and Hydropower Generator. *Aiaa J.* **2011**, *49*, 1374–1386. [CrossRef]
9. Kinsey, T.; Dumas, G. Optimal Tandem Configuration for Oscillating-Foils Hydrokinetic Turbine. *J. Fluids Eng.* **2012**, *134*, 031103. [CrossRef]
10. Young, J.; Ashraf, M.A.; Lai, J.C.S.; Platzer, M.F. Numerical Simulation of Fully Passive Flapping Foil Power Generation. *Aiaa J.* **2013**, *51*, 2727–2739. [CrossRef]
11. Kim, J.; Kim, D.G.; Jung, S.; Moon, S.M.; Ko, J.H. Experimental study of a fully passive flapping hydrofoil turbine with a dual configuration and a coupling mechanism. *Renew. Energy* **2023**, *208*, 191–202. [CrossRef]
12. Kim, D.G.; Kim, J.; Ko, J.H. An experimental investigation of the performance of a power transmission mechanism for a flapping-foil hydrokinetic turbine. *Renew. Energy* **2024**, *237*, 121636. [CrossRef]
13. Veilleux, J.C.; Dumas, G. Numerical optimization of a fully-passive flapping-airfoil turbine. *J. Fluids Struct.* **2017**, *70*, 102–130. [CrossRef]
14. Duarte, L.; Dellinger, N.; Dellinger, G.; Ghenaim, A.; Terfous, A. Flapping Foil Hydrokinetic Turbine: From a Strongly Coupled FSI Solver to the Experiment in a Confined Channel. In *Proceedings of the Advances in Critical Flow Dynamics Involving Moving/Deformable Structures with Design Applications, Santorini, Greece, 18–22 June 2018*; Braza, M., Hourigan, K., Triantafyllou, M., Eds.; Springer: Cham, Switzerland, 2021; pp. 315–325.
15. Duarte, L.; Dellinger, N.; Dellinger, G.; Ghenaim, A.; Terfous, A. Experimental investigation of the dynamic behaviour of a fully passive flapping foil hydrokinetic turbine. *J. Fluids Struct.* **2019**, *88*, 1–12. [CrossRef]
16. Boudreau, M.; Picard-Deland, M.; Dumas, G. A parametric study and optimization of the fully-passive flapping-foil turbine at high Reynolds number. *Renew. Energy* **2020**, *146*, 1958–1975. [CrossRef]

17. Theodorakis, K.; Ntouras, D.; Papadakis, G. Investigation of a submerged fully passive energy-extracting flapping foil operating in sheared inflow. *J. Fluids Struct.* **2021**, *113*, 103674. [CrossRef]
18. Duarte, L.; Dellinger, N.; Dellinger, G.; Ghenaim, A.; Terfous, A. Experimental optimisation of the pitching structural parameters of a fully passive flapping foil turbine. *Renew. Energy* **2021**, *171*, 1436–1444. [CrossRef]
19. Huxham, G.H.; Cochard, S.; Patterson, J. Experimental Parametric Investigation of an Oscillating Hydrofoil Tidal Stream Energy Converter. In Proceedings of the 18th Australasian Fluid Mechanics Conference, Launceston, Australia, 3–7 December 2012; p. 4.
20. Karbasian, H.; Esfahani, J.; Barati, E. The power extraction by flapping foil hydrokinetic turbine in swing arm mode. *Renew. Energy* **2016**, *88*, 130–142. [CrossRef]
21. Sitorus, P.E.; Ko, J.H. Power extraction performance of three types of flapping hydrofoils at a Reynolds number of 1.7E6. *Renew. Energy* **2019**, *132*, 106–118. [CrossRef]
22. Sitorus, P.E.; Le, T.Q.; Ko, J.H.; Truong, T.Q.; Park, H.C. Design, implementation, and power estimation of a lab-scale flapping-type turbine. *J. Mar. Sci. Technol.* **2016**, *21*, 115–128. [CrossRef]
23. Liu, Z.; Qu, H.; Shi, H. Energy-harvesting performance of a coupled-pitching hydrofoil under the semi-passive mode. *Appl. Energy* **2020**, *267*, 114889. [CrossRef]
24. Liu, Z.; Qu, H.; Zhang, G. Experimental and numerical investigations of a coupled-pitching hydrofoil under the fully-activated mode. *Renew. Energy* **2020**, *155*, 432–446. [CrossRef]
25. Cloutier, D.; Olivier, M.; Dumas, G. Parametric Study of a Fully Passive Oscillating Foil on a Swinging Arm. *Energies* **2025**, *18*, 1277. [CrossRef]
26. Zhao, F.; Jiang, Q.; Wang, Z.; Qadri, M.N.M.; Li, L.; Tang, H. Interaction of two fully passive flapping foils arranged in tandem and its influence on flow energy harvesting. *Energy* **2023**, *268*, 126714. [CrossRef]
27. Wang, G.; Ng, B.F. Energy harvesting performance of a tandem-hydrofoil based closely-interconnected tidal array. *Energy Convers. Manag.* **2023**, *280*, 116796. [CrossRef]
28. Zhao, F.; Wang, Z.; Qadri, M.N.M.; Khan, O.; Munir, A.; Shahzad, A.; Tang, H. Effects of wake interaction on energy extraction performance of tandem semi-active flapping foils. *Phys. Fluids* **2023**, *35*, 087112. [CrossRef]
29. Qu, H.l.; Liu, Z. Numerical Study on the Energy Extraction Performance of Coupled Tandem Flapping Hydrofoils. *China Ocean. Eng.* **2022**, *36*, 38–49. [CrossRef]
30. Naccache, G.; Paraschivoiu, M. Development of the Dual Vertical Axis Wind Turbine Using Computational Fluid Dynamics. *J. Fluids Eng.* **2017**, *139*, 121105. [CrossRef]
31. Naccache, G.; Paraschivoiu, M. Parametric study of the dual vertical axis wind turbine using CFD. *J. Wind. Eng. Ind. Aerodyn.* **2018**, *172*, 244–255. [CrossRef]
32. Siemens Digital Industries Software. *Simcenter STAR-CCM+ User Guide, v.2021.2*; Siemens Digital Industries Software: Plano, TX, USA, 2021.
33. Spalart, P.; Rumsey, C. Effective Inflow Conditions for Turbulence Models in Aerodynamic Calculations. *Am. Inst. Aeronaut. Astronaut.* **2007**, *45*, 2544–2553. [CrossRef]
34. Polyak, B. Some methods of speeding up the convergence of iteration methods. *Ussr Comput. Math. Math. Phys.* **1964**, *4*, 1–17. [CrossRef]
35. Ruder, S. An overview of gradient descent optimization algorithms. *arXiv* **2016**. [CrossRef]
36. Newman, B. Multiple actuator-disc theory for wind turbines. *J. Wind. Eng. Ind. Aerodyn.* **1986**, *24*, 215–225. [CrossRef]


**Disclaimer/Publisher's Note:** The statements, opinions and data contained in all publications are solely those of the individual author(s) and contributor(s) and not of MDPI and/or the editor(s). MDPI and/or the editor(s) disclaim responsibility for any injury to people or property resulting from any ideas, methods, instructions or products referred to in the content.